University of Vermont
UVM ScholarWorks

Graduate College Dissertations and Theses | Dissertations and Theses

2021

Two-Dimensional Bose–Hubbard Model for Helium on Graphene

Jiangyong Yu
University of Vermont

Follow this and additional works at: https://scholarworks.uvm.edu/graddis

 Part of the Condensed Matter Physics Commons

Recommended Citation

Yu, Jiangyong, "Two-Dimensional Bose–Hubbard Model for Helium on Graphene" (2021). *Graduate College Dissertations and Theses*. 1463.
https://scholarworks.uvm.edu/graddis/1463

This Thesis is brought to you for free and open access by the Dissertations and Theses at UVM ScholarWorks. It has been accepted for inclusion in Graduate College Dissertations and Theses by an authorized administrator of UVM ScholarWorks. For more information, please contact donna.omalley@uvm.edu.

TWO-DIMENSIONAL BOSE-HUBBARD MODEL FOR HELIUM ON GRAPHENE

A Thesis Presented

by

Jiangyong Yu

to

The Faculty of the Graduate College

of

The University of Vermont

In Partial Fullfillment of the Requirements
for the Degree of Master of Science
Specializing in Physics

August, 2021

Defense Date: June 21st, 2021.
Thesis Examination Commitee:

Valeri Kotov, Ph.D, Advisor
Bernard (Chip) Cole, Ph.D, Chairperson
Adrian Del Maestro, Ph.D
Taras Lakoba, Ph.D
Cynthia J. Forehand, Ph.D, Dean of the Graduate College

Abstract

An exciting development in the field of correlated systems is the possibility of realizing two-dimensional (2D) phases of quantum matter. For a systems of bosons, an example of strong correlations manifesting themselves in a 2D environment is provided by helium adsorbed on graphene. We construct the effective Bose-Hubbard model for this system which involves hard-core bosons ($U \approx \infty$) and repulsive nearest-neighbor ($V > 0$) interactions.

In this work, we focus on the calculations of single particle properties of the model such as the hopping parameter t. This is accomplished via Wannier Theory and Band structure calculations, which proves to be reliable methods of calculating such properties. For the many body properties such as V, we show that Wannier Theory breaks down and other methods are preferably used. The result places the ground state of the first layer of ^{4}He adsorbed on graphene deep in the commensurate solid phase with 1/3 of the sites on the dual triangular lattice occupied

Citation

Material from this thesis has been has been published in the following form:

Yu, J., Lauricella, E., Elsayed, M., Shepherd, K., Nichols, N. S., Lombardi, T., Kim, S. W., Wexler, C., Vanegas, J. M., Lakoba, T., Kotov, V. N., and Del Maestro, A.. Two-dimensional bose-hubbard model for helium on graphene. Phys. Rev. B **103**, 235414 (2021).
`https://link.aps.org/doi/10.1103/PhysRevB.103.235414`

Acknowledgments

This thesis would not have been possible without the help of some incredible people.

I would like to thank my advisors, Professor Adrian Del Maestro and Professor Valeri Kotov, for always being available to help despite their busy schedules and for sharing their experiences and knowledge with me.

I would like to thank the other members of the Del maestro group and VTSGC Research team for always providing me assistance when asked, especially Hatem Bargathi, who helped guide me with my first forays into research, and made the experience so much less daunting that it should have been.

I would also like to thank my parents, for all ways supporting me through my life with school any everything else.

This work was supported, in part, under NASA grant number 80NSSC19M0143. Computational resources were provided by the NASA High-End Computing (HEC) Program through the NASA Advanced Supercomputing (NAS) Division at Ames Research Center.

Table of Contents

Chapter 1

Introduction

This chapter contains sections and figures from the following published work by the author [1].

1.1 Backgrounds and Motivation

The problem of Helium-4(^{4}He) atoms deposited on solid substrates has been identified for many decades as a bosonic many-body problem that could exhibit a rich phase diagram[2, 3, 4, 5, 6, 7, 8, 9]. Because ^{4}He atoms are neutral, the many-body interactions that determine the behavior of this system are the van der Waals (VDW) interactions between He atom pairs and between He and the Carbon atoms in graphite. Specifically, the attractive VDW interaction between He atom pairs tends to be weaker than the attractive VDW interaction between He atoms and other atoms. This means that He is a universal wetting agent and easily spreads over most surfaces [10]. This behavior in which atoms forms a thin layer on top of a substrate is called adsorption. Since VDW interactions are typically fairly weak, but long range, the possibility of superfluidity, and at which density (and film coverage) it can exist depends on the interplay between the two-body He–He interactions and the interaction of He with the

substrate atoms. Graphite, a bulk material made up of many layers of carbon atoms in hexagonal lattices, was initially used due to its exceptional homogeneity [11]. Extensive experimental [12, 13] and theoretical studies [14, 15, 16] have demonstrated that under the right circumstances a superfluid He film can develop on the second layer of He adsorbed on graphite. The reason that a superfluid He film does not developer on the first layer is because of the stronger adorption potential closer to the layer, which strongly localizes the He atoms. However, the discovery of the two-dimensional (2D) version of graphite, namely graphene [17](essentially a single layer of the hexagonal lattice of carbon atoms in graphite), with a 10% weaker adsorption potential, has lead to the possibility of purely 2D ^{4}He superfluidity (atomic width film) in the first layer of He adsorbed on graphene [18, 19, 6, 20]. Furthermore, if superfluidity does not exist on the first layer of He adsorbed on graphene, the 2D nature of graphene also lets us more easily manipulate graphene in a variety of ways [21, 17, 22] and change the adsorption potential between He and graphene [18]. This could provide another path to realize the existence of a 2D superfluidity in He absorbed on graphene.

1.1.1 Nasa Relevance

Great advances have been made in the experimental field of cold atoms. Since the first creation of a Bose-Einstein condensate in 1995 [23], cold atom experiments have reached such low temperatures and momenta that the force of gravity has begun to have an effect on the construction and measurements of cold atom experiments. This was one of the main motivations of the creation of Nasa's Cold Atom Lab (CAL). Located on the Internation Space Station, the CAL allows cold atom experiments to be done in microgravity, conditions difficult to replicate on earth [24]. The microgravity enviroment allows exper-

imentalists to explore novel quantum materials in a regime called the "coldest place in the universe", and the theoretical framework developed in this thesis can help to guide further studies in this area. By establishing a Bose-Hubbard model frameworks for exploring 2D quantum phases, we can pinpoint interesting 2D systems that can then be explored by experimentalists on earth or in space.

1.2 Model: Helium on Graphene

First, let us describe the behavior of ^{4}He adsorbing on pristine graphene in vacuum. When He is deposited on graphene, the VDW interactions between the He atoms and the substrate forms a honeycomb shaped potential, in which the minimum of the interaction is located above the centers of each of the graphene hexagons. Thus, the deposited He atoms occupy the sites in the center of each graphene hexagon that forms a triangular lattice. However, the He-He VDW interaction is repulsive at the length between the sites on the triangular lattice as show in Fig. 1.3, so the He will first fill 1/3 of the triangular lattice sites such that no two adjacent sites are filled at the same time. This forms the the so-called C1/3 commensurate solid as show in Fig. 1.1. As one continues to add particles, the He atoms will fill up to 2/3 of the sites, or form a second layer, and so on. So far, theoretical studies [19, 25, 26, 27, 20] have confirmed the existence of the insulating C1/3 commensurate solid state.

Now let us describe the geometry of the system of He adsorped on graphene. First, the graphene lattice is made up of carbon atoms fixed at $z = 0$ forming a hexagonal lattice with lattice ($\boldsymbol{a}$) and basis ($\boldsymbol{b}$) vectors:

$$\begin{aligned} \boldsymbol{a}_1 &= \frac{a_0}{2}\big(\sqrt{3}, 3\big), \quad & \boldsymbol{b}_1 &= \frac{a_0}{2}\big(\sqrt{3}, 1\big) \\ \boldsymbol{a}_2 &= \frac{a_0}{2}\big(-\sqrt{3}, 3\big), \quad & \boldsymbol{b}_2 &= a_0(0, 1) \end{aligned} \tag{1.1}$$

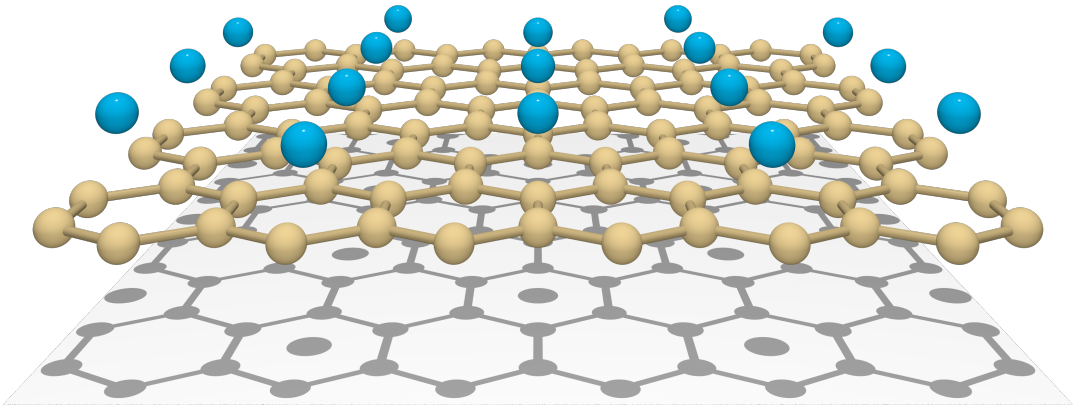

Figure 1.1: A schematic of the $\sqrt{3} \times \sqrt{3}$ commensurate solid phase for ^{4}He atoms (blue) adsorbed on graphene (gold) showing 1/3 of the $N_{\hexagon} = 72$ sites filled where the He atoms are localized on the sites of a triangular lattice (see shadow). The size of the indicated region of graphene is $L_x \times L_y \simeq 22\,\text{Å} \times 17\,\text{Å}$.

At some height z, which is determined by the He-graphene adsorption potential, above the graphene lattice, the sites occupied by the He atoms forms a triangular lattice with the same lattice vectors ($\boldsymbol{a}$) as the graphene lattice. These lattices, as well as the relevant quantities which we will calculate, are shown in Fig. 1.2.

1.3 The Bose-Hubbard Model

The aim of this work is to develop an effective 2D Bose–Hubbard (BH) model for the first layer of ^{4}He on graphene. The reason that such a model is desirable is that a BH model allows us to identify the important interactions that determine the phase of the system of He adsorped on graphene. This allows us to theoretically predict the phase of systems of He adsorped on graphene and tell us what manipulations of the graphene substrate could lead to 2D superfluidity. This could even be generalized to other 2D systems of similar form. The Hamiltonian for such a Bose–Hubbard model is:

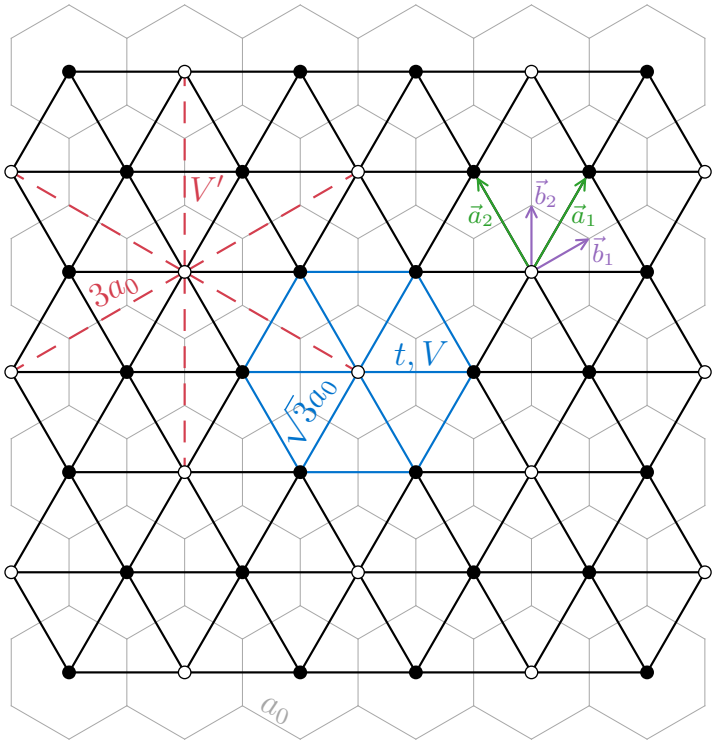

Figure 1.2: The triangular lattice defined by hexagon centers of the graphene lattice (shown in grey) with the lattice and basis vectors in Eq. (1.1) shown in the upper right. The nearest neighbor hopping t and interaction V are experienced between sites separated by $\sqrt{3}a_0$ (blue) where $a_0 \simeq 1.42\,\text{Å}$ is the length of a hexagon side. The dashed red lines indicate the next-nearest neighbor interaction V' between sites separated by $3a_0$ which form a triangular superlattice at 1/3 filling (open circles) which corresponds to the adsorbed C1/3 solid depicted in Fig. 1.1. Lattice vectors $\boldsymbol{a}_1$ and $\boldsymbol{a}_2$ are shared between the graphene and triangular lattice.

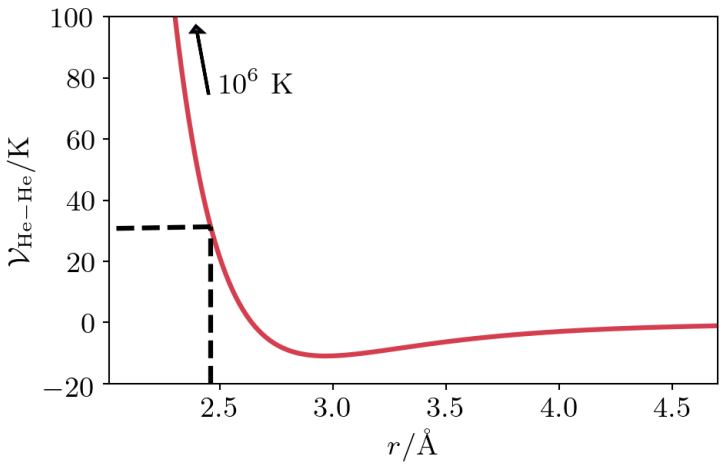

Figure 1.3: The interaction potential between two Helium atoms in Kelvin, plotted against the distance between two Helium atoms r in Angstroms. At zero distance the repulsive interaction is on the order of 10^6 Kelvin. At the distance between two Helium sites of $\sqrt{3}a_0$ or about 2.46 Angstroms, the interaction potential is still about 31 Kelvin. The minimum of the potential is only about -9 Kelvin at about 2.8 Angstrom.

$$H_{BH} = -t\sum_{\langle i,j\rangle}(b_i^\dagger b_j + h.c.) + V\sum_{\langle i,j\rangle} n_i n_j + V'\sum_{\langle\langle i,j\rangle\rangle} n_i n_j + \dots. \tag{1.2}$$

In this model, t is the hopping strength, which indicates how likely an He atom absorbed on a site will hop the a site next to it. V and V' are the strengths of the nearest neighbor and next-nearest neighbor interaction. The operators $b_i^\dagger(b_i)$ creates (destroys) a bosonic ^{4}He atom on site i with $[b_i, b_j^\dagger] = \delta_{i,j}$ and $n_i = b_i^\dagger b_i$ counts the number of particle on site i. The sites i, j correspond to the vertices of the triangular lattice formed by the centers of graphene's hexagons as seen in Fig. 1.2. The brackets in $\langle i, j\rangle$ and $\langle\langle i, j\rangle\rangle$ indicates restrictions to the sum such that only the nearest neighbor sites and next-nearest neighbor sites are summed over, respectively. The ellipsis indicates higher order interactions that are neglected here. Absent from our BH Hamiltonian the the on site interation term U, which is common to many Hubbard models. The reason that we have

omitted U is the fact that the separation of our lattice sites is on the same length scale as the strong repulsive core of the He-He VDW interaction. The strength of this repulsive interaction at zero lengths is at a scale (10^6 K) much larger than the relevant interactions we are trying to capture with the Bose-Hubbard Model, so we must omit the on site interaction term U and preclude the possibility of multiple He atoms occupying the same site. As such, our Bose-Hubbard model is a Hard-Core Bose-Hubbard model. As mentioned above, the He-He interaction remains quite repulsive even at the length scale of one lattice vector as show in Fig. 1.3, this will cause difficulty in the calculations of the BH parameters, and lead to the multitude of approaches that we take in this work.

1.4 Approach

A system of N ^{4}He atoms of mass m interacting with the graphene substrate can be described in first quantization via the Hamiltonian:

$$H = -\frac{\hbar^2}{2m}\sum_{i=1}^{N}\nabla_i^2 + \sum_{i=1}^{N}\mathcal{V}_{\mathrm{He-G}}(\boldsymbol{r}_i) + \sum_{i<j}\mathcal{V}_{\mathrm{He-He}}(\boldsymbol{r_i} - \boldsymbol{r_j}) \tag{1.3}$$

where the i^{th} atom is located at position $\boldsymbol{r}_i = (x_i, y_i, z_i)$. The interaction between helium atoms is $\mathcal{V}_{\mathrm{He-He}}$, shown in Fig. 1.4(a), while the corrugated helium–graphene potential $\mathcal{V}_{\mathrm{He-G}}$ can be constructed empirically [28, 29, 30, 31, 32, 33, 34, 25, 35]. Here, we employ the form of Ref. [28], obtained from the sum of isotropic interactions between ^{4}He and C atoms with the 6–12 Lennard–

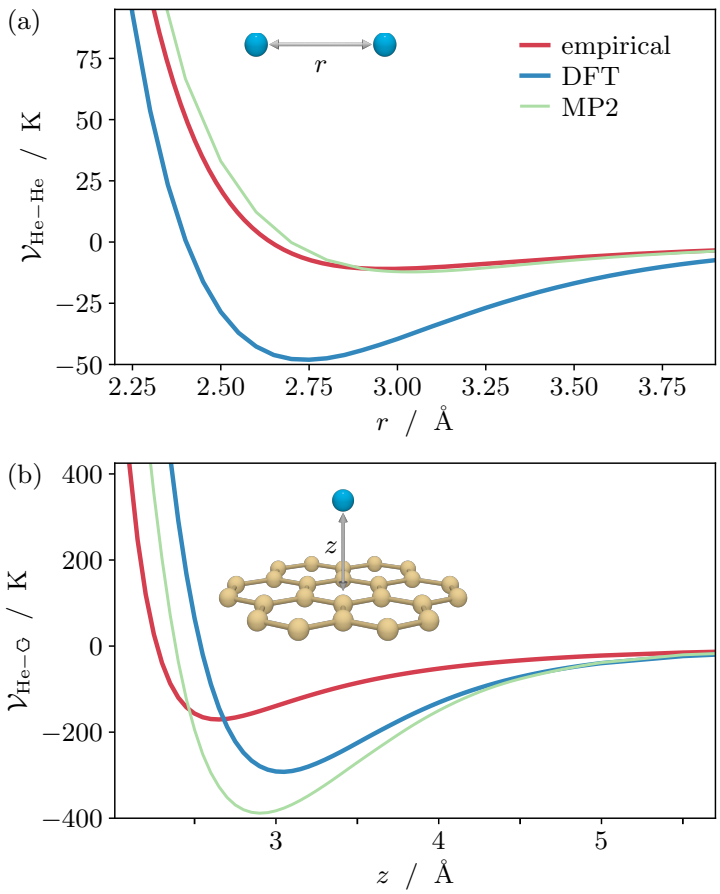

Figure 1.4: The interaction (a) and adsorption (b) potentials in Eq. (1.3). The three curves in both panels indicate three different approaches to the potentials. Empirical indicates the formulas discussed in the text where $\mathcal{V}_{\mathrm{He-He}}$ is taken from Ref. [36] while $\mathcal{V}_{\mathrm{He-G}}$ is determined from Eq. (1.4) at $\boldsymbol{\imath} = (0, 0)$. The potentials labelled DFT and MP2 are extracted from the minimal energy surfaces determined by those ab initio methods as described in § 4.1 and 4.2.

Jones potential with parameters σ and ε:

$$\mathcal{V}_{\mathrm{He-G}}(\boldsymbol{r}_i) = \varepsilon\sigma^2 \frac{4\pi}{A} \left\{ \left[\frac{2}{5} \left(\frac{\sigma}{z_i} \right)^{10} - \left(\frac{\sigma}{z_i} \right)^{4} \right] + \sum_{\boldsymbol{g}\neq 0} \sum_{\ell=1}^{2} \mathrm{e}^{\imath \boldsymbol{g}\cdot(\boldsymbol{\imath}_i - \boldsymbol{b}_\ell)} \left[\frac{1}{60} \left(\frac{g\sigma^2}{2z_i} \right)^{5} K_5(gz_i) - \left(\frac{g\sigma^2}{2z_i} \right)^{2} K_2(gz_i) \right] \right\} . \quad (1.4)$$

In Eq. (1.4), $\boldsymbol{\imath}_i = (x_i, y_i)$ are the coordinates of a ^{4}He atom in the xy-plane, $\boldsymbol{b}_\ell$ are the basis vectors defined in Eq. (1.1), $\boldsymbol{g}$ are the reciprocal lattice vectors,

defined as

$$\boldsymbol{g} = n_1\boldsymbol{G}_1 + n_2\boldsymbol{G}_2 \tag{1.5}$$

$$\boldsymbol{G}_1 = \frac{2\pi}{3a_0}\Big(\sqrt{3}, 1\Big), \qquad \boldsymbol{G}_2 = \frac{2\pi}{3a_0}\Big(-\sqrt{3}, 1\Big), \tag{1.6}$$

We start with calculating the one particle properties using the empirical potential Eq. (1.6). First, density of the first layer in z is determined by solving the 1D Schrodinger equation using the shooting method for the average of the empirical potential in $x - y$. The 3D He-graphene VDW potential Eq. (1.6) is then averaged in z, weighted by the density in z, to produce a 2D potential. This 2D potential is then solved numerically using Bloch's theorem to produce a band structure and Bloch states. In order to compute the hopping t we employ the maximally localized Wannier functions, which are single-particle wave functions constructed from the Bloch states, and tight binding calculations. The maximally localized Wannier function can also be used to calculate two particle interaction parameters like V and V'. However, due to the aforementioned strong repulsion of $\mathcal{V}_{\mathrm{He-He}}$ at low distances and the disregarding of said potential in the Wannier calculations, unphysically large results are obtained. Methods that take into account the He-He interactions must be employed to obtain physical values of V and V'.

Two methods are employed using the empirical potential to incorporate the influence of $\mathcal{V}_{\mathrm{He-He}}$. First is the self-consistent Hartree-Fock equations [37, 38]. Which uses variational methods to take into account the He-He interactions. Second, the path integral ground state quantum Monte Carlo (QMC) method is employed to simulate He atoms above a Graphene sheet.

Two types of ab initio methods are also employed: Density Functional The-

Method	t / (K)	V / (K)	V' / (K)	t/V
Wannier	1.45	7540	638	0.0002
HF	1.45	69.7	-2.08	0.021
QMC	1.38	54.3(1)	-2.76(2)	0.025
DFT	1.10	21.4	-1.36	0.051
MP2	0.59	51.5	-1.97	0.011

Table 1.1: The hopping parameter t, nearest and next nearest-neighbor interaction V and V', and the ratio of t/V of the effective Bose–Hubbard model defined in Eq. (1.2) as calculated by the five different methods: Wannier functions, Hartree–Fock (HF), quantum Monte Carlo (QMC), Density Functional Theory (DFT), and Møller–Plesset perturbation theory (MP2). In all cases, t is calculated via the band structure of single helium atom subject to a periodic two-dimensional adsorption potential $\mathcal{V}_{\mathrm{He-C}}$. Note that t is the same for Wannier and Hartree–Fock as they use the same empirical potential.

ory (DFT) [39, 40] improved by including VDW energies in the appropriate DFT functional [41, 42, 43], and 2nd order Møller–Plesset (MP2) [44, 45, 46]. In all cases, the He-graphene adsorption potential can be determined, and the hopping t can then be extracted from the bandwidth or overlap integrals. The adsorption and He-He potential for all methods are shown in Fig.1.4. The resulting values of t, V, and V' are show in Table.1.1.

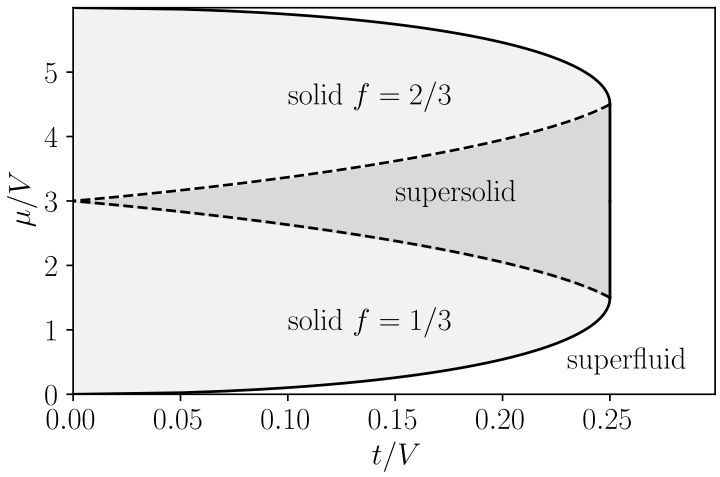

Figure 1.5: The mean-field phase diagram for hard-core bosons on the triangular lattice with nearest-neighbor interactions V and hopping t with density controlled by the chemical potential μ. Identified phases include commensurate solids (at fillings $f = 1/3, 2/3$), superfluid, and supersolid (a superfluid that breaks triangular lattice symmetries). Solid lines indicate discontinuous (first order) transitions, while continuous (second order) transitions occur across dashed lines. The data points in the lower left-hand corner represent the major results of this paper, indicating that the ground state of a single layer of ^{4}He on graphene resides deep in the commensurate solid phase at 1/3 filling.

1.5 The Bose-Hubbard Phase Diagram

The phase diagram of Eq. (1.2) considering only nearest neighbor interactions ($t - V$ model) can be analyzed within the mean-field theory [47, 48], is shown in Fig. 1.5. This result is known to be in qualitative agreement with lattice quantum Monte Carlo for hard-core bosons with extended interactions [49, 50, 51]. The axis are in terms of the two parameters explained above, t and V, and the chemical potential μ. The chemical potential can be thought of as the average energy per particle of a system and governs the exchange of particles between systems. When two systems are in contact, particles will move from the system with higher chemical potential to the one with lower potential [52]. This can be used to control the number of particles in a system by connecting the system to a reservoir whose chemical potential we can control. For the system of

He on Graphene, the chemical potential can be thought of as the partial pressure of the He gas that is adsorbing onto the graphene sheet. For small values of the chemical potential (low filling fraction) three phases are identified: the C1/3 phase discussed previously, a supersolid phase, and uniform superfluid phase, in order of increasing hopping t. At higher values of the chemical potential, a C2/3 phase exists, though we will not explore this phase.

1.6 Outline

The rest of the Thesis are set up as follows. The second chapters describes the process of determining the position in z of He adsorbing on graphene. The shooting method is employed to solve the Schrodinger equation in 1D, and the 3D empirical potential is reduced to a 2D one. The third chapter contains the sum of all empirical calculations. First, the full mapping of the 2D Bose-Hubbard model is described. Then, we describe the full detail of the calculations of t through Bloch theorem and Wannier functions, both for empirical and ab initio adsorption potentials. Then the two empirical methods of correctly calculating V, Hartree-Fock and Quantum Monte Carlo, are described. The fourth chapter contains the description of the ab initio calculation of V via Density Functional Theory and Møller–Plesset. The final chapter contains the discussion of results and potential future work.

Chapter 2

Dimensionality of the First Layer

This chapter contains sections and figures from the following published work by the author [1]. The author's contribution includes utilizing the shooting method to find the density in z of the first layer of Helium abosrbed on graphene.

2.1 Dimensionality of the First Adsorbed Layer

Regardless of the form of the employed interaction potential in the microscopic model, the goal of this work is to obtain access to properties of the ground state of the N-particle three-dimensional time-independent Schrödinger equation:

$$H\Psi_0(\boldsymbol{R}) = E_0\Psi_0(\boldsymbol{R}) \tag{2.1}$$

in order to determine the parameters of an effective two-dimensional Bose–Hubbard Hamiltonian described by Eq. (1.2) where $\boldsymbol{R} \equiv \{\boldsymbol{r}_1, \ldots, \boldsymbol{r}_N\}$ are the spatial locations of helium atoms.

The basic physical picture of adsorption of helium on graphene is clear. At low temperature and densities, atoms preferentially adsorb to the strong binding sites located at the center of graphene hexagons due to the attractive interaction seen in Fig. 1.4(b). If the density is low enough that interactions between helium atoms are not relevant, Eq. (1.3) can be numerically integrated to obtain the z-dependence of the wavefunction in the approximation where the corrugation is neglected and the atoms experience an average smooth potential over the xy-plane. This potential, which we will call $\mathcal{V}_0$ from now, is obtained by taking only the $\boldsymbol{g} = 0$ term in Eq. (1.4).

$$\mathcal{V}_0(z) = \varepsilon\sigma^2 \frac{4\pi}{A} \left\{ \left[\frac{2}{5} \left(\frac{\sigma}{z} \right)^{10} - \left(\frac{\sigma}{z} \right)^4 \right] \right. \tag{2.2}$$

This potential can then be used to solve the 1D Schrodinger equation in z, allowing us to obtain the density distribution of the first layer in z.

2.2 Shooting Method

The shooting method is a numerical method that allows us to find solutions to differential equations in 1D provided that we know the boundary conditions. It can be a good way to numerically solve for bound state solutions to the Schrodinger equation in 1D. The main challenge in utilizing the shooting method is intelligently choosing the initial conditions, following which the procedure is routine. Let us start with the Schrodinger equation in 1D:

$$\left[-\frac{\hbar}{2m} \frac{\partial^2}{\partial x^2} + (V(x) - E) \right] \psi(x) = 0 \tag{2.3}$$

for which we know the potential $V(x)$ within some interval $x_0 < x < x_1$. For most potentials, we have a reasonable intuition of the expected solution to the Schrodinger equation based on the properties of the Schrodinger equation and

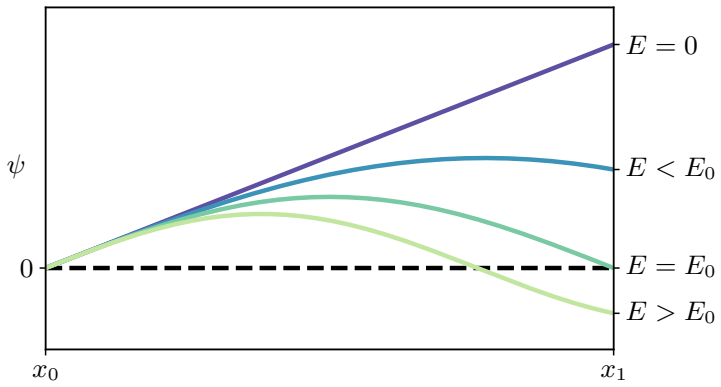

Figure 2.1: An example of several shooting method wavefunctions for the case of the square well, where the potential is 0 in the interval shown and ∞ elsewhere. The wavefunction is expected to be 0(shown as the black dashed line) at both x_0 and x_1. We start with $E = 0$ and gradually increase the energy until the wavefunction that we "shot" from the left matches the boundary conditions at the right.

differential equations in general. Using this intuition we make a "guess" for the values of $\psi(x_0)$, $\psi'(x_0)$, and $\psi(x_1)$. We then set the value of E to the minimum value of $V(x)$, knowing that the energy for bound states cannot be less than the minimum of $V(x)$. Using the inital values of $\psi(x_0)$ and $\psi'(x_0)$, we solve Eq. (2.3) step-by-step using a numerical method such as the Runge-Kutta method until we arrive at $x = x_1$. We now check to see if the numerical solution $\psi_s(x_1)$ matches the predetermined "guess" $\psi(x_1)$. If they do not match, we increase the energy E slightly and repeat the preceding steps. If they do, or very nearly does, we have arrived at a solution. When the shooting method finds a solution, it is not guaranteed that the solution found is the ground state. This can be checked by visually inspecting the wavefunction ψ, if it only has one node, the ground state solution is found, if it has multiple nodes, some intermediate eigenvalue E might have been skipped. The accuracy of the solution is bound by the accuracy of the numerical calculations. If the shooting method is found not to converge, one may increase the accuracy of the numerical calculations by going from the Euler method to the second order Runge-Kutta method, for

example, or increasing the precision of the floating point numbers used to store the calculations. The process of arriving at the ground state solution for the square well is show in Fig. 2.1.

2.2.1 Examples of choosing boundary values

Let us consider the application of the shooting method to two simple and well know models for the Schrodinger Equation. First, the infinite square well:

$$V(x) = \begin{cases} 0, & x_0 < x < x_1 \\ \infty, & \text{elsewhere.} \end{cases} \tag{2.4}$$

We know from the infinite V at the edge of the box that $\psi(x_0) = \psi(x_1) = 0$. We also know from the discontinuities in V that $\psi'(x_0)$ is some finite value. In general, when $\psi'(x_0)$ is expected to be finite, $\psi'(x_0)$ is set to 1 (or any other small number of your liking), as changing $\psi'(x_0)$ will only change the normalization of the solution ψ.

Now let us consider the case of the harmonic oscillator:

$$V(x) \propto x^2. \tag{2.5}$$

The boundary conditions in this case are less obvious. While we expect $\psi(x) \to 0$ as $x \to \infty$, we cannot set our boundaries at infinity. We can attempt to set our boundary at some large number far from the origin, but setting $\psi'(x)$ then becomes difficult as $\psi'(x) \to 0$ as $x \to \infty$ also. We cannot set both $\psi(x)$ and $\psi'(x)$ to 0 as that would give us the trivial solution. However, we can exploit the even parity of the potential to give us the boundary conditions. Since $V(x)$ is an even function, we know that the eigenfunctions to the Schrodinger equation must be either even or odd. Knowing this, we can solve for the solutions in

two sets. We will first set $x_0 = 0$. For the even solutions, we set $\psi(x_0) = 1$ and $\psi(x_0)' = 0$. Once more the exact value for the non-zero guess is not important, as it will only affect the normalization. For the odd solutions we set $\psi(x_0) = 0$ and $\psi(x_0)' = 1$. To set x_1 we can use the fact that $\psi(x) \to 0$ as $x \to \infty$. We can set x_1 to some large number, and set $\psi(x_1) = 0$. It is important to keep $E \ll V(x_1)$ for our guess at x_1 to remain valid, thus if the eigenvalues found are large compared to $V(x_1)$, x_1 must be increased.

The first 4 solutions to the two cases outline above are show in Fig. 2.2.

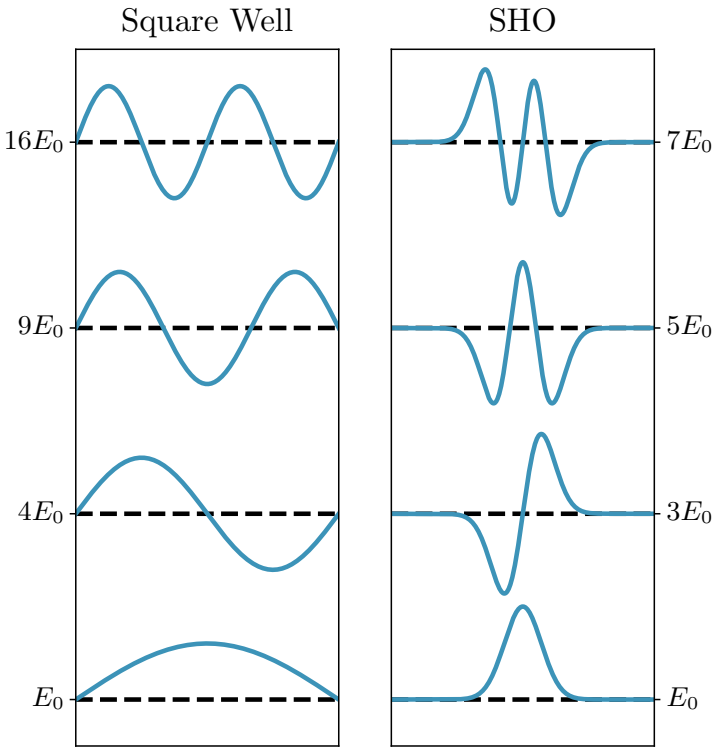

Figure 2.2: The first 4 solution to the square well and simple harmonic oscillator found via the shooting method. The black dashed lines indicate $\psi = 0$ for each wavefunction. The wavefunctions and energies match the well known analytical solutions. The energies are shown in multiples of the ground state energy E_0 and accurate to within 4 significant figures.

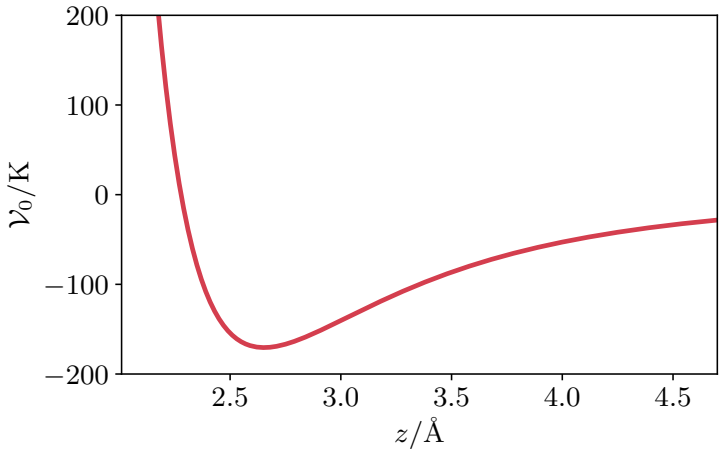

Figure 2.3: The average adsorption potential $\mathcal{V}_0$ for the empirical potential. The minimum of -170.5 K occurs at z = 2.64 Å.

2.2.2 Applications to He on Graphene

In our case, the average potential experienced by the adsorbed atoms is $V_0(z)$ above the graphene layer, as shown in Fig. 2.3. The behaviors of a single atom above the layer in z is thus governed by the following 1D time-independent Schrodinger equation:

$$\left[-\frac{\hbar}{2m}\frac{\partial^2}{\partial z^2} + (\mathcal{V}_0(z) - E)\right]\psi(z) = 0. \tag{2.6}$$

$\mathcal{V}_0$ forms a potential well with a minimum $-170K$, $\mathcal{V}_0$ becomes large as $z \to 0$ and approaches zero as $z \to \infty$. Unfortunately, neither of the examples provided above will help us in determining the boundary conditions, as there are no infinity or any symmetry in the potential. We will have to use our intuition to make reasonable guesses for the boundary conditions. We can expect that $\psi \to 0$ as $z \to 0$, so we set $z_1 = 0$ and $\psi(z_1) = 0$. We also expect $\psi \to 0$ as $z \to \infty$, in this case, we choose a large enough z_0, in our case $z_0 = 10$, such that $V(z_0) \approx 0$, and set $\psi(z_0) = 0$. Since $\mathcal{V}_0(z_1) << \mathcal{V}_0(z_0)$, we expect the derivative of the wavefunction to be greater at z_0 and so we start the shooting method from z_0, setting $\psi'(z_0) = 1$.

2.3 Shooting Method Results

The resulting single particle density in the z-direction [53, 54, 19] is shown in Fig. 2.4 along with values corresponding to the adsorption potentials computed via ab initio methods. Thus, single atoms are strongly localized around $z \approx 3\,\text{Å}$,

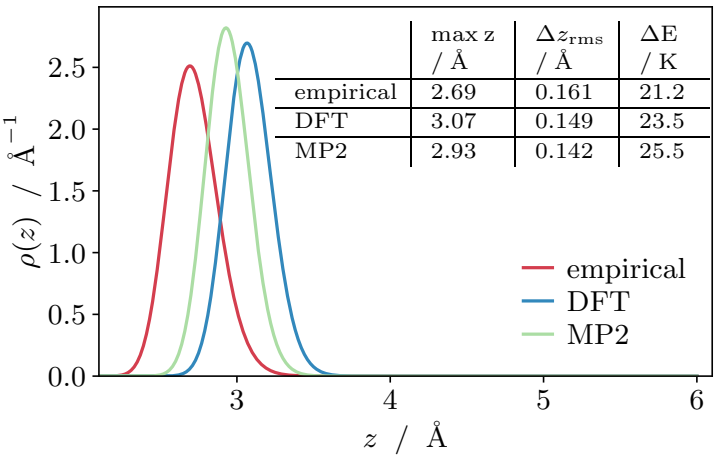

Figure 2.4: The particle density, $\rho(z) \propto |\phi_0(z)|^2$ in Eq. (**??**) obtained via the shooting method for $\mathcal{V}_{\text{He}-\text{G}}$ computed for the three different approaches to the potentials described in § **??**-**??**. The table indicates the value of z at which the maximum density occurs, the root mean squared value of z $\Delta z_{\text{rms}} = \sqrt{\langle z^2 \rangle - \langle z \rangle^2}$, and the difference between the zero point energy and the minimum of $\mathcal{V}_{\text{He}-\text{G}}$ for each potential. All three methods yield density profiles for the adsorbed layer that are effectively two dimensional with sub-angstrom widths.

regardless of the way the adsorption potential is calculated, with an root mean squared width of $\approx 0.15\,\text{Å}$ and a zero point energy that lifts the ground state $\approx 20\,\text{K}$ above the classical potential minimum.

As the density of atoms is increased, there is now a competition between the energy gained due to attraction of the graphene sheet, and the interaction potential between helium atoms, $\mathcal{V}_{\text{He}-\text{He}}$, which has an attractive minimum at $r_{\text{min}} \approx 3\,\text{Å}$ and eventually becomes repulsive at smaller distances (see Fig. 1.4). The length scales defining $\mathcal{V}_{\text{He}-\text{He}}$ should be compared with those imposed by the graphene corrugation potential where the nearest neighbor distance be-

tween two hexagon centers is $\ell_{\rm NN} = \sqrt{3}a_0 \simeq 2.46\,\text{Å}$ while the next-nearest neighbor distance, corresponding to one out of every three hexagons occupied has $\ell_{\rm NNN} = 3a_0 \simeq 4.26\,\text{Å}$ as seen in Fig. 1.2. Thus at low densities, the system stabilizes at a single well-defined 2D monolayer, that can exist at both commensurate and incommensurate filling fractions $f = N/N_{\rm G}$ (where $N_{\rm G}$ is the number of triangular lattice sites) in a regime of coverage where both the adsorption and interaction energies are attractive. As the density continues to increase, eventually the cost of repulsive interactions between helium atoms overcomes the reduced attraction felt further from the sheet and layer completion is reached near $f \approx 0.6$. At this point, a second layer begins to form and the system can no longer be considered as effectively two dimensional (see Fig. 3.11 in § 3.5.2).

This simple picture has been validated by 50 years of experiments [2, 55, 4, 56, 57, 58, 59] and numerical simulations [14, 54, 15, 60, 25, 26, 61, 35, 16] on helium adsorbed on graphite, where the adsorption potential is 10% stronger than graphene. While no experiments yet exist in the graphene system considered here, quantum Monte Carlo simulations [19, 26, 62, 63, 20, 64, 65] both at zero and finite temperature show analogous behavior. As already discussed in the introduction, in the first layer, a commensurate $\sqrt{3} \times \sqrt{3}$ R 30° incompressible C1/3 solid phase (helium atoms occupy 1/3 of the strong binding sites on a triangular lattice (hexagon centers) with constant $\sqrt{3}a_0$ and axes rotated by 30° with respect to the original graphene triangular lattice) is thermodynamically stable over a large range of chemical potentials [20] (see Figs. 1.1 and 1.2) and may compete with a lower density liquid [64] depending on simulation details and the employed form of $\mathcal{V}_{He-\rm G}$. All observed phases in the first layer are incompressible, with no systematic evidence of finite superfluid density surviving extrapolation to the thermodynamic limit.

Thus, the ground state of the first adsorbed monolayer of ^{4}He on graphene can be described by an effective two-dimensional system. We now discuss how it can be mapped at low energies onto a single-band Bose–Hubbard model, which requires moving beyond the simple continuum one-body model described here and understanding the role of interactions in Eq. (1.3).

Chapter 3

Empirical methods

This chapter contains sections and figures from the following published work by the author [1], The author's contribution to this section includes calculating the hopping matrix element t for all methods via the Bloch theorem and Wannier functions.

3.1 Effective 2D Bose–Hubbard Description

We attack the problem of building the 2D Bose-Hubbard model at various levels of sophistication starting from the non-interacting band structure and Wannier theory, then systematically explore the effects of interactions in different approximation schemes: Hartree, Hartree–Fock, quantum Monte Carlo, Møller–Plesset and dispersion corrected density functional theory.

In this section we introduce an effective 2D $\mathcal{V}_{\mathrm{He-C}}(\boldsymbol{\imath})$ potential where $\boldsymbol{\imath} = (x, y)$ is the in-plane coordinate. The way $\mathcal{V}_{\mathrm{He-C}}(\boldsymbol{\imath})$ is determined depends on the specific method used and will be discussed on a case by case basis.

3.1.1 Mapping onto a Bose–Hubbard Model

First, we outline the well-known general procedure for mapping the interacting problem in Eq. (1.3), onto the effective Bose–Hubbard model Eq. (1.2). This mapping is valid at low energies and therefore the two representations lead to the same ground state properties. A similar mapping has been used to analyze the properties of dilute Bose gases confined on optical lattices [66, 67, 68]; however the physics in our case turns out to be fundamentally different due to the importance of short-range correlations for a (fairly dense) collection of helium atoms confined to the graphene lattice.

We begin by expressing the first-quantized microscopic Hamiltonian in Eq. (1.3) in second quantization for a single 2D monolayer, via the introduction of bosonic field operators, $\hat{\Psi}(\boldsymbol{\rho}), \hat{\Psi}^\dagger(\boldsymbol{\rho})$ such that the local density is $n(\boldsymbol{\rho}) = \hat{\Psi}^\dagger(\boldsymbol{\rho})\hat{\Psi}(\boldsymbol{\rho})$. In this notation, the effective 2D Hamiltonian can be written as a sum of a one-particle term, which includes the kinetic energy and the helium–graphene potential, and a two-body term (that originates from the helium–helium interaction) [69, 70]:

$$\begin{aligned} H &= \int \mathrm{d}\boldsymbol{\rho}\hat{\Psi}^\dagger(\boldsymbol{\rho})\Big(-\frac{\hbar^2}{2m}\nabla^2_{\boldsymbol{\rho}} + \mathcal{V}_{\mathrm{He-G}}(\boldsymbol{\rho})\Big)\hat{\Psi}(\boldsymbol{\rho}) + \\ &\quad \frac{1}{2}\iint \mathrm{d}\boldsymbol{\rho}\mathrm{d}\boldsymbol{\rho}'\, \hat{\Psi}^\dagger(\boldsymbol{\rho})\hat{\Psi}^\dagger(\boldsymbol{\rho}')\mathcal{V}_{\mathrm{He-He}}(\boldsymbol{\rho}-\boldsymbol{\rho}')\hat{\Psi}(\boldsymbol{\rho}')\hat{\Psi}(\boldsymbol{\rho})\,, \end{aligned} \tag{3.1}$$

where a discussion of $\mathcal{V}_{\mathrm{He-He}}$ is included in Appendix A of [1]. For helium atoms strongly confined near 2D triangular lattice locations $\boldsymbol{\rho}_i$ defined by the centers of graphene hexagons (see Fig. 1.2), the field operators can be expanded over a complete orthonormal set of localized Wannier functions $\psi(\boldsymbol{\rho}-\boldsymbol{\rho}_i)$ and the bosonic annihilation and creation operators $b_i, b_i^\dagger$ [69, 70]:

$$\hat{\Psi}(\boldsymbol{\rho}) = \sum_{\boldsymbol{\rho}_i} \psi(\boldsymbol{\rho}-\boldsymbol{\rho}_i)b_i, \quad \hat{\Psi}^\dagger(\boldsymbol{\rho}) = \sum_{\boldsymbol{\rho}_i} \psi^*(\boldsymbol{\rho}-\boldsymbol{\rho}_i)b_i^\dagger. \tag{3.2}$$

We use the shorthand notation $b_i^\dagger \equiv b_{\boldsymbol{r}_i}^\dagger$ for an operator that creates a boson at $\boldsymbol{r}_i$, and $\psi_i(\boldsymbol{r}) = \psi(\boldsymbol{r} - \boldsymbol{r}_i)$ for the Wannier function localized around the site i on a triangular lattice. With $n_i = b_i^\dagger b_i$ being the number of particles at the site i. The Wannier functions will be constructed in the next section, and we assume that they correspond to the lowest energy band.

Substituting Eq. (3.2) into Eq. (3.1) one obtains:

$$\begin{aligned} H = \int \mathrm{d}\boldsymbol{r} \sum_i \psi_i{}^*(\boldsymbol{r}) b_i^\dagger \Big(-\frac{\hbar^2}{2m} \nabla_{\boldsymbol{r}}^2 + \mathcal{V}_{\mathrm{He-C}}(\boldsymbol{r}) \Big) \sum_j \psi_j(\boldsymbol{r}) b_j + \\ \frac{1}{2} \iint \mathrm{d}\boldsymbol{r} \mathrm{d}\boldsymbol{r}' \sum_i \psi_i^*(\boldsymbol{r}) b_i^\dagger \sum_j \psi_j^*(\boldsymbol{r}') b_j^\dagger \mathcal{V}_{\mathrm{He-He}}(\boldsymbol{r} - \boldsymbol{r}') * \\ \sum_k \psi_k(\boldsymbol{r}') b_k \sum_l \psi_l(\boldsymbol{r}) b_l \,. \end{aligned} \tag{3.3}$$

We can pull out all the sums and the bosonic annihilation and creation operators.

$$\begin{aligned} H = \sum_{i,j} b_i^\dagger b_j \int \mathrm{d}\boldsymbol{r} \psi_i^*(\boldsymbol{r}) \Big(-\frac{\hbar^2}{2m} \nabla_{\boldsymbol{r}}^2 + \mathcal{V}_{\mathrm{He-C}}(\boldsymbol{r}) \Big) \psi_j(\boldsymbol{r}) + \\ \frac{1}{2} \sum_{i,j,k,l} b_i^\dagger b_j^\dagger b_k b_l \iint \mathrm{d}\boldsymbol{r} \mathrm{d}\boldsymbol{r}' \, \psi_i^*(\boldsymbol{r}) \psi_j^*(\boldsymbol{r}') \mathcal{V}_{\mathrm{He-He}}(\boldsymbol{r} - \boldsymbol{r}') \psi_k(\boldsymbol{r}') \psi_l(\boldsymbol{r}) \,. \end{aligned} \tag{3.4}$$

We can then take advantage of the orthonormality of the Wannier functions:

$$\int \mathrm{d}\boldsymbol{r} \psi_i^*(\boldsymbol{r}) \psi_j(\boldsymbol{r}) = \delta_{i,j}, \tag{3.5}$$

and use integration by parts to obtain:

$$
\begin{aligned}
H &= \sum_{i,j} b_i^\dagger b_j \int \mathrm{d}\boldsymbol{r}\psi_i^*(\boldsymbol{r})\left(-\frac{\hbar^2}{2m}\nabla_{\boldsymbol{r}}^2 + \mathcal{V}_{\mathrm{He-G}}(\boldsymbol{r})\right)\psi_j(\boldsymbol{r}) + \\
&\quad \frac{1}{2}\sum_{i,j} n_i n_j \iint \mathrm{d}\boldsymbol{r}\mathrm{d}\boldsymbol{r}' \, |\psi_i(\boldsymbol{r})|^2 \mathcal{V}_{\mathrm{He-He}}(\boldsymbol{r}-\boldsymbol{r}')|\psi_j(\boldsymbol{r}')|^2. \qquad (3.6)
\end{aligned}
$$

This can be mapped to the effective lattice Bose–Hubbard Hamiltonian in Eq. (1.2). In both sums over i and j, the summand approaches zero rapidly as the sites represented by i and j gets further apart. The first term of the Hamiltonian becomes a constant when $i = j$, thus the largest term of interest is when i and j are nearest neighbors, this is the one-particle hopping (t). The second term of the Hamiltonian consists of a sum containing successively smaller interaction parameters starting with the on-site (U), nearest-neighbor (V), and next-nearest-neighbor (V') on a triangular lattice, determined by the distance between i and j. Thus we can extract the standard expressions for these paramters[70]:

$$
\begin{aligned}
t &= -\int \mathrm{d}\boldsymbol{r}\psi^*(\boldsymbol{r})\left[-\frac{\hbar^2}{2m}\nabla_{\boldsymbol{r}}^2 + \mathcal{V}_{\mathrm{He-G}}(\boldsymbol{r})\right]\psi(\boldsymbol{r}-\boldsymbol{a}_1) && (3.7)\\
U &= \iint \mathrm{d}\boldsymbol{r}\mathrm{d}\boldsymbol{r}' \, |\psi(\boldsymbol{r})|^2 \mathcal{V}_{\mathrm{He-He}}(\boldsymbol{r}-\boldsymbol{r}')|\psi(\boldsymbol{r}')|^2 && (3.8)\\
V &= \iint \mathrm{d}\boldsymbol{r}\mathrm{d}\boldsymbol{r}' \, |\psi(\boldsymbol{r})|^2 \mathcal{V}_{\mathrm{He-He}}(\boldsymbol{r}-\boldsymbol{r}')|\psi(\boldsymbol{r}'-\boldsymbol{a}_1)|^2 && (3.9)\\
V' &= \iint \mathrm{d}\boldsymbol{r}\mathrm{d}\boldsymbol{r}' \, |\psi(\boldsymbol{r})|^2 \mathcal{V}_{\mathrm{He-He}}(\boldsymbol{r}-\boldsymbol{r}')|\psi(\boldsymbol{r}'-\boldsymbol{a}_1-\boldsymbol{a}_2)|^2. && (3.10)
\end{aligned}
$$

Here, the choice of lattice site for the computation is arbitrary due to translational invariance, and one can replace $\boldsymbol{a}_1 \leftrightarrow \boldsymbol{a}_2$.

3.2 Band Structure and Effective Hopping t

In order to calculate the overlap integrals in Eqs. (3.7)–(3.10), we start by evaluating the general band structure and specifically the hopping parameter t which are determined by the purely one-particle Hamiltonian,

$$-\frac{\hbar^2}{2m}\nabla_{\boldsymbol{r}}^2 + \mathcal{V}_{\text{He}-\text{C}_{60}}(\boldsymbol{r}). \tag{3.11}$$

We must find the solutions to the one-particle Schrodinger equation with this Hamiltonian, and then construct the band structure and Wannier functions.

3.2.1 Bloch's Theorem

We start with the 2D Schrodinger equation, labeled by band n and quasi-momentum k,

$$\left[\frac{p^2}{2m} + \mathcal{V}_{\text{He}-\text{C}_{60}}(\boldsymbol{r})\right]\Psi_k^{(n)}(\boldsymbol{r}) = E_k^{(n)}\Psi_k^{(n)}(\boldsymbol{r}), \tag{3.12}$$

where $p = -i\hbar\left(\frac{\partial}{\partial x} + \frac{\partial}{\partial y}\right)$, the 2D momentum operator, and $\boldsymbol{k}$ is the 2D quasi-momentum within the Brillouin zone in momentum space. Bloch's theorem states that the solution to the Schrodinger equation for a periodic potential must take the following form

$$\Psi_k^{(n)}(\boldsymbol{r}) = e^{i\boldsymbol{k}\cdot\boldsymbol{r}}u_k^{(n)}(\boldsymbol{r}). \tag{3.13}$$

This solution takes the form of a plane wave $e^{i\boldsymbol{k}\cdot\boldsymbol{r}}$ multiplied by a periodic function $u_k^{(n)}(\boldsymbol{r})$ with the same periodicity as the potential. In our case, $u_k^{(n)}(\boldsymbol{r}) = u_k^{(n)}(\boldsymbol{r}+\boldsymbol{a}_1) = u_k^{(n)}(\boldsymbol{r}+\boldsymbol{a}_2)$. We can then substitute Eq. (3.13) into Eq. (3.12) to obtain:

$$\left[\frac{1}{2m}(p+\hbar k)^2+\mathcal{V}_{\mathrm{He-G}}(\boldsymbol{z})\right]u_k^{(n)}(\boldsymbol{z})=E_k^{(n)}u_k^{(n)}(\boldsymbol{z}). \tag{3.14}$$

We can easily extract the Fourier components of Eq. $\mathcal{V}_{\mathrm{He-G}}(\boldsymbol{z})$ in (1.4) such that $\mathcal{V}_{\mathrm{He-G}}(\boldsymbol{z})=\sum_{\mathbf{g}} c_{\mathbf{g}} * e^{i\mathbf{g}\cdot\boldsymbol{z}}$, they are:

$$c_{\mathbf{g}}=\sum_{\ell=1}^{2}\mathrm{e}^{-\imath\boldsymbol{g}\cdot\boldsymbol{b}_\ell}\left[\frac{1}{60}\left(\frac{g\sigma^2}{2z_i}\right)^5 K_5(gz_i)-\left(\frac{g\sigma^2}{2z_i}\right)^2 K_2(gz_i)\right]. \tag{3.15}$$

Similarily, we can also expand the periodic functions $u_k^{(n)}(\boldsymbol{z})$ in Fourier Modes:

$$u_k^{(n)}(\boldsymbol{z})=\sum_{\mathbf{g}} C_{\mathbf{g}}^{(n,q)}e^{i\mathbf{g}\cdot\boldsymbol{z}}. \tag{3.16}$$

Now subsituting the expanded Fourier series into Eq. (3.17) and rescaling by the recoil energy $E_R=\frac{\hbar^2G^2}{2m}$, where G is the length of either of the reciprocal lattice vectors in Eq. (1.6).

$$\sum_{\mathbf{g}}\left[E_R\left(\frac{\mathbf{g}}{G}+\frac{k}{G}\right)^2+\sum_{\mathbf{g}'}c_{\mathbf{g}'}e^{i\mathbf{g}'\cdot\boldsymbol{z}}\right]C_{\mathbf{g}}^{(n,k)}e^{i\mathbf{g}\cdot\boldsymbol{z}}=\sum_{\mathbf{g}}E_k^{(n)}C_{\mathbf{g}}^{(n,k)}e^{i\mathbf{g}\cdot\boldsymbol{z}}. \tag{3.17}$$

Combining the exponents of $\mathbf{g}$ and $\mathbf{g}'$ in the left hand side.

$$\sum_{\mathbf{g}}\left[E_R\left(\frac{\mathbf{g}}{G}+\frac{k}{G}\right)^2 C_{\mathbf{g}}^{(n,k)}e^{i\mathbf{g}\cdot\boldsymbol{z}}+\sum_{\mathbf{g}'}c_{\mathbf{g}'}C_{\mathbf{g}}^{(n,k)}e^{i(\mathbf{g}'+\mathbf{g})\cdot\boldsymbol{z}}\right]=\sum_{\mathbf{g}}E_k^{(n)}C_{\mathbf{g}}^{(n,k)}e^{i\mathbf{g}\cdot\boldsymbol{z}}. \tag{3.18}$$

Let's rearrange the outer sum over $\mathbf{g}$ such that the value in the exponent in the inner sum is always $e^{i(\mathbf{g})}$ in stead of $e^{i(\mathbf{g})}$ or $e^{i(\mathbf{g}'+\mathbf{g})}$:

$$\sum_{\mathbf{g}}e^{i\mathbf{g}\cdot\boldsymbol{z}}\left[E_R\left(\frac{\mathbf{g}}{G}+\frac{k}{G}\right)^2 C_{\mathbf{g}}^{(n,k)}+\sum_{\mathbf{g}'}c_{\mathbf{g}'}C_{\mathbf{g}-\mathbf{g}'}^{(n,k)}\right]=\sum_{\mathbf{g}}e^{i\mathbf{g}\cdot\boldsymbol{z}}E_k^{(n)}C_{\mathbf{g}}^{(n,k)}. \tag{3.19}$$

We can then define the Hamiltonian:

$$H_{\mathbf{g},\mathbf{g}''} = \left[E_R \left(\frac{\mathbf{g}}{G} + \frac{k}{G} \right)^2 \delta_{\mathbf{g},\mathbf{g}''} + \sum_{\mathbf{g}'} c_{\mathbf{g}'} \delta_{\mathbf{g},\mathbf{g}''-\mathbf{g}'} \right], \tag{3.20}$$

to simplify the equation to:

$$\sum_{\mathbf{g}''} H_{\mathbf{g},\mathbf{g}''} C^{(n,k)}_{\mathbf{g}''} = E^{(n)}_k C^{(n,k)}_{\mathbf{g}}. \tag{3.21}$$

The resulting Hamiltonian is a 4D matrix which must be reshaped into a 2D matrix and then diagonalized numerically, in our case using MATLAB's eigs function.

3.2.2 Numerical Calculations of Bloch States

During the numerical calculations, we performed a change of variables, shown in Fig. 3.1, that aligned the lattice vectors $\boldsymbol{a}_1$ and $\boldsymbol{a}_2$ with our new axis and set the period of the lattice from $\sqrt{3}a_0$ to π,

$$\begin{aligned} x_{lat} &= \frac{\pi}{2}x + \frac{\sqrt{3}\pi}{2}y \\ y_{lat} &= -\frac{\pi}{2}x + \frac{\sqrt{3}\pi}{2}y. \end{aligned} \tag{3.22}$$

Now the unit vectors for the lattice and reciprocal lattice are:

$$\begin{aligned} \boldsymbol{a}_1 &= (\pi, 0) \qquad \boldsymbol{a}_2 = (0, \pi), \\ \boldsymbol{G}_1 &= (2, 0) \qquad \boldsymbol{G}_2 = (0, 2). \end{aligned} \tag{3.23}$$

This makes it possible to perform the calculations, as in Cartesian coordinates the unit cells are not actually periodic in y. Since we will perform integrations for t and V in this coordinate system, we must remember to include the Jacobian determinant in the integrand.

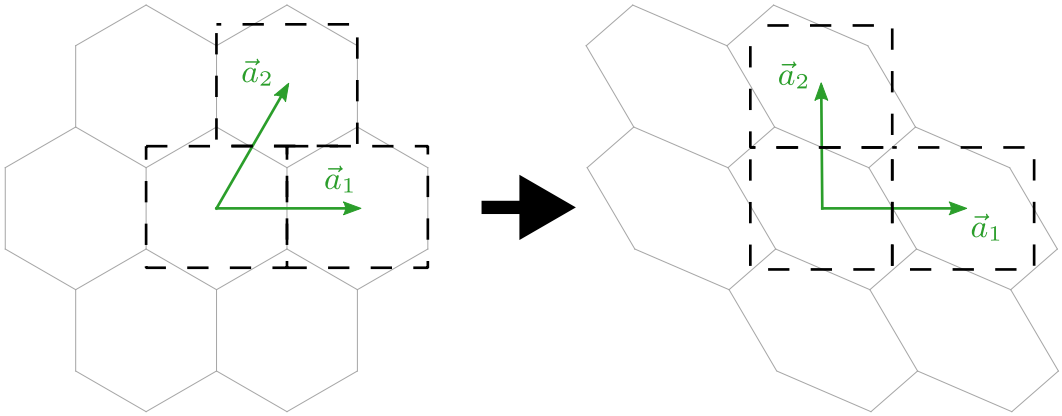

Figure 3.1: Visual demonstration of the change of basis performed. The axis has been rotated by 60 deg so that the geometry of the new basis is more clear. This made it so that the lattice is now periodic along our new axis x_{lat} and y_{lat}.

$$|\mathbf{J}| = \begin{vmatrix} \frac{1}{2} & -\frac{1}{2} \\ \frac{\sqrt{3}}{2} & \frac{\sqrt{3}}{2} \end{vmatrix} = \frac{\sqrt{3}}{2} \tag{3.24}$$

Then, for each k within the Brillouin zone, we construct the Hamiltonian Eq. (3.20), reshape it to a 2D matrix and solve it to obtain: $C_{\mathbf{g}}^{(n,k)}$ as a vector. The eigenvalues can be used to form the band structure 3.4. The eigenstates are then reshaped back to a matrix in $\mathbf{g}$ and combined via Eq. (3.16) to form the periodic functions $u_k^{(n)}(\boldsymbol{r})$. These are then combined by Eq. (3.13) to form the Bloch wavefunctions $\Psi_k^{(n)}(\boldsymbol{r})$. Since we are only interested in the first band, from now on we will assume $n = 1$ and drop the band index (n).

3.2.3 Wannier Function

Once the Bloch wave-functions $\Psi_k(\boldsymbol{r})$ are found, the localized Wannier functions are constructed via

$$\psi_i(\boldsymbol{r}) = \psi(\boldsymbol{r} - \boldsymbol{r}_i) = \frac{1}{\sqrt{N_\hexagon}} \sum_{\boldsymbol{k} \in BZ} \mathrm{e}^{-i\boldsymbol{k}\cdot\boldsymbol{r}_i} \Psi_{\boldsymbol{k}}(\boldsymbol{r}), \tag{3.25}$$

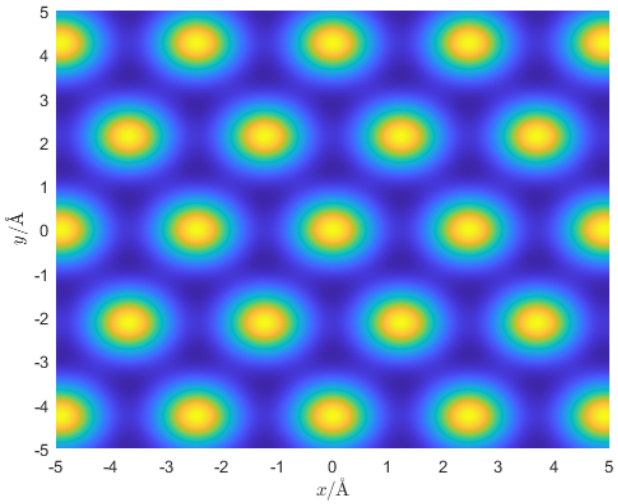

Figure 3.2: Periodic part of bloch wavefunction $u_k^{(1)}(\boldsymbol{\rho})$ for $k = 0$. Also $\Psi_k^{(1)}(\boldsymbol{\rho})$ for $k = 0$.

where the summation is over the first Brillouin zone, and $N_{\hexagon}$ is the number of (triangular) lattice sites. As mentioned above, the Wannier function is both orthogonal to the Wannier function on any other site and normalized, i.e., $\int \mathrm{d}\boldsymbol{\rho}\psi_i^*\psi_j = \delta_{i,j}$. This means the Wannier function is a good representation of a single He atom localized to one site. Eq. (3.25) can now be used in the overlap integral for t defined in Eq. (3.7) for a given value of $\mathcal{V}_{\mathrm{He}-\hexagon}$ computed within the empirical or ab initio approach. The Wannier function calculated from the empirical Bloch theorem calculations is show in Fig. 3.3

3.2.4 Empirical

Here the bare potential is given by Eq. (1.4) and we use two approaches to construct an effective 2D potential $\mathcal{V}_{\mathrm{He}-\hexagon}(\boldsymbol{\rho})$.

Following the discussion in § 2.1, we can integrate the full 3D helium–graphene interaction potential over the probability density in the z-direction presented in Fig. 2.4 as described in detail in Appendix A of [1]. This leads to a 2D potential $\widetilde{\mathcal{V}}_{\mathrm{He}-\hexagon}(\boldsymbol{\rho})$ as defined in Eq. (**??**). Expressed as an integral, this

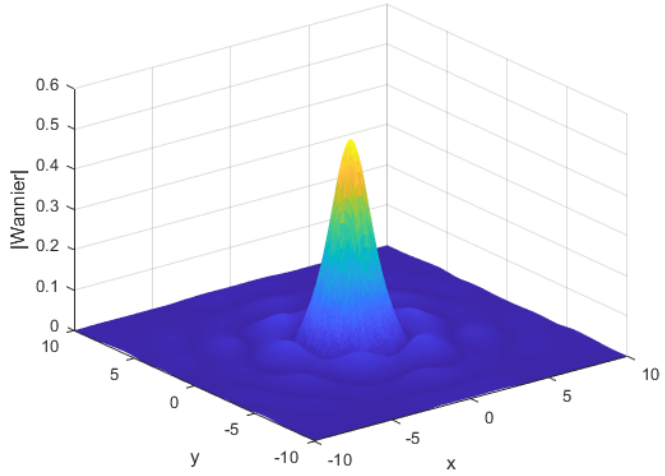

Figure 3.3: Surface plot of the calculated Wannier function for the first layer of Helium on Graphene. The majority of the wavefunction forms a large bump centered at the site $\boldsymbol{\imath}_i = (0, 0)$, and the six smaller bumps near the large bump roughly corresponds to the six Helium sites near the central site.

is:

$$\widetilde{\mathcal{V}}_{\text{He}-\text{G}}(\boldsymbol{\imath}) = \int \mathrm{d}z\, \mathcal{V}_{\text{He}-\text{G}}(\boldsymbol{r})\rho(z). \tag{3.26}$$

The corresponding band structure is presented in Fig. 3.4 and a cut of the resulting Wannier function is plotted in Fig. 3.5(a). Based on these results, Eq. (3.7) is evaluated in the lowest band resulting in:

$$t_{\text{W}} = 1.45\,\text{K}\,. \tag{3.27}$$

In addition, we can approximate the lowest band via tight binding. In tight binding, the energy of the lowest band is:

$$\varepsilon(\boldsymbol{k}) = \int \mathrm{d}\boldsymbol{\imath}\Psi^{\dagger}(\boldsymbol{\imath})H\Psi(\boldsymbol{\imath}), \tag{3.28}$$

where the Bloch functions can be constructed from the Wannier functions as:

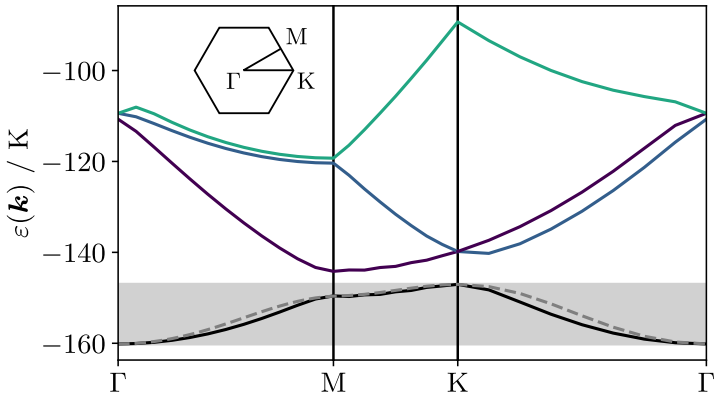

Figure 3.4: The band structure obtained using $\widetilde{\mathcal{V}}_{\mathrm{He-C_{60}}}(\boldsymbol{r})$ as introduced Eq. (**??**) along a high symmetry path in the first Brillouin zone as shown in the inset. The first band (in black) is well separated from the higher excited bands and thus the low energy properties of the system are determined by the lowest band. The dashed line shows the tight binding dispersion from Eq. (3.33), in excellent agreement with the continuum model supporting the use of an effective 2D lattice model. The shaded region corresponds to the bandwidth equal to $9t$ as determined symmetry.

$$\Psi_{\boldsymbol{k}}(\boldsymbol{r}) = \frac{1}{\sqrt{N_{\mathrm{C_{60}}}}} \sum_i \mathrm{e}^{i\boldsymbol{k}\cdot\boldsymbol{r}_i} \psi_i(\boldsymbol{r}). \tag{3.29}$$

Subsituting Eq. (3.29) in to Eq. (3.28) we get:

$$\varepsilon(\boldsymbol{k}) = \frac{1}{N_{\mathrm{C_{60}}}} \sum_{i,j} \int \mathrm{d}\boldsymbol{r} \mathrm{e}^{i\boldsymbol{k}\cdot(\boldsymbol{r}_j - \boldsymbol{r}_i)} \psi_j^*(\boldsymbol{r}) H \psi_i(\boldsymbol{r}). \tag{3.30}$$

The $i = j$ term forms ε_0 :

$$\varepsilon_0 = \int \mathrm{d}\boldsymbol{r} \psi^*(\boldsymbol{r})_i H \psi(\boldsymbol{r})_i, \tag{3.31}$$

and the remaining terms(excluding any non nearest-neighbor) form:

$$\varepsilon(\boldsymbol{k}) - \varepsilon_0 = \sum_{\langle i,j \rangle} \mathrm{e}^{i\boldsymbol{k}\cdot(\boldsymbol{r}_j - \boldsymbol{r}_i)} \int \mathrm{d}\boldsymbol{r} \psi_i^*(\boldsymbol{r}) H \psi_j(\boldsymbol{r}). \tag{3.32}$$

The integral on the right is by definition $-t$, and the restrictions on i and j

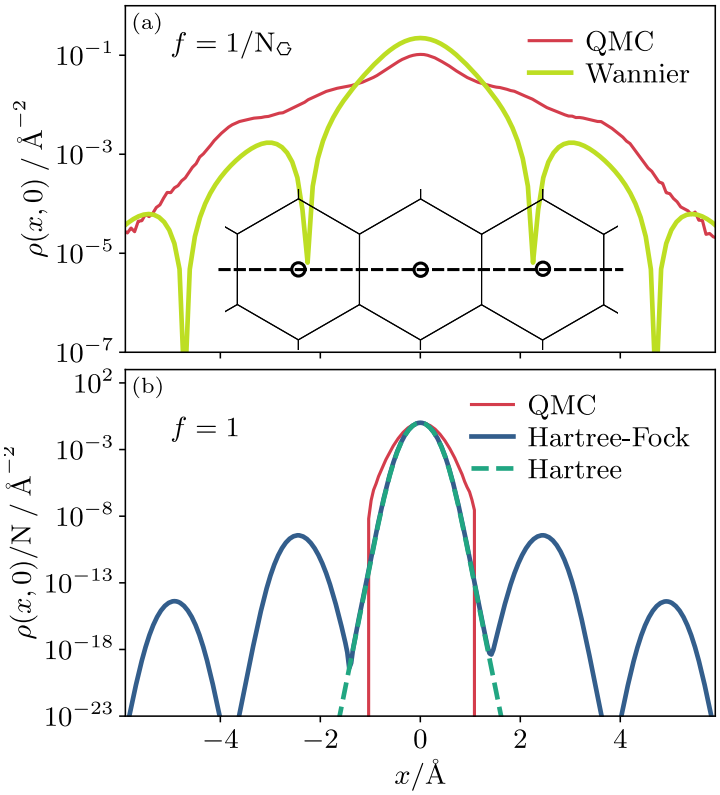

Figure 3.5: Spatial dependence of the density $\rho(x, y) = |\psi(x, y)|^2/N$ of an adsorbed ^{4}He atom on graphene for a $y = 0$ cut in the xy-plane corresponding to the lattice path shown in the top inset. (a) A comparison of the localized Wannier function defined in Eq. (3.25) to that computed via quantum Monte Carlo (QMC) for a single particle $N = 1$, $f = 1/N_{\hexagon}$ by slightly biasing a single site at the level of the trial wavefunction as discussed in § 3.5. The wavefunction strongly penetrates into neighboring lattice sites, leading to the breakdown of Wannier theory for the computation of interaction parameters. (b) The density at unit filling $N = N_{\hexagon}$ as computed via QMC, and within the Hartree-Fock and Hartree approximations showing the tendency towards exponential localization on a single site. In both panels, the 2D normalization is computed over the full graphene sheet.

means $\boldsymbol{\rho}_j - \boldsymbol{\rho}_i = [\boldsymbol{a}_1, \boldsymbol{a}_2, -\boldsymbol{a}_1, -\boldsymbol{a}_2, \boldsymbol{a}_1 - \boldsymbol{a}_2, \boldsymbol{a}_2 - \boldsymbol{a}_1]$, meaning the exponents take the form of three standing waves in the direction of the three smallest $\mathbf{k}$ vectors. These can be simplified to cosines in terms of k_x and k_y. Thus:

$$\varepsilon(\boldsymbol{k}) - \varepsilon_0 = -2t\left[\cos(k_x a) + 2\cos\left(\frac{k_x a}{2}\right)\cos\left(\frac{\sqrt{3}k_y a}{2}\right)\right], \tag{3.33}$$

where $a = \sqrt{3}a_0$ and ε_0 is an energy offset. This means that the bandwidth, defined as the energy difference between the K point (located at momentum $(4\pi/3a, 0)$) and the Γ point $(0, 0)$ in Fig. 3.4, is equal to $9t$. Equation (3.33) is plotted as the dashed line in Fig. 3.4, and the considerable agreement provides further validation for mapping from the continuum to a lattice model.

An alternative approach to obtaining a 2D effective potential is to exactly simulate a single ^{4}He atom subject to the full 3D potential via quantum Monte Carlo as described in detail in § 3.5 and obtain the adsorption potential as a function of the 2D coordinate in the plane, $\boldsymbol{\rho}$, via Eq. (3.47): $\mathcal{V}_{\text{He}-\text{G}}(\boldsymbol{\rho}) = \langle \mathcal{V}_{\text{He}-\text{G}}(x, y) \rangle$. This potential is then used to calculate t using the method described in the next section. The corresponding hopping parameter calculated from this potential is

$$t_{\text{QMC}} = 1.38(1)\,\text{K}. \tag{3.34}$$

where the parenthesis indicates the statistical uncertainty in the last digit. We note that this value agrees with that computed using the adsorption potential determined from the 1D wavefunction in Eq. (3.27) at the order of 10%.

3.2.5 Ab Initio

The hopping parameter t can also be estimated for an effective 2D potential computed within the ab initio approximation. While it is computationally difficult to perform a DFT and MP2 calculation for every position $\boldsymbol{\rho}$, these

numerical methods can readily determine the adsorption potential at the high symmetry points corresponding to the minima, maxima, and saddle point (as shown in Fig. 3.6).

Since the summation over $|\boldsymbol{g}|$ is dominated by the terms with the smallest magnitudes and converges rapidly, the full 2D potential can be approximated as

$$\mathcal{V}_{\text{He}-\text{C}_6}(\boldsymbol{z}) = \mathcal{V}_0 + c_{g_1} \sum_{|\boldsymbol{g}|=g_1} \mathrm{e}^{i\boldsymbol{g}\cdot\boldsymbol{z}} + c_{g_2} \sum_{|\boldsymbol{g}|=g_2} \mathrm{e}^{i\boldsymbol{g}\cdot\boldsymbol{z}}, \tag{3.35}$$

where $g_1 = 4\pi/(3a_0)$ and $g_2 = \sqrt{3}g_1$ are the lengths of the two smallest set of $\boldsymbol{g}$ vectors . The coefficients $c_{g_{1,2}}$ can be uniquely determined from the minimum, maximum, and saddle point values of the potential. We define the positions of the minimum, maximum, and saddle point as $\boldsymbol{z}_{\text{min}} = (0,0)$, $\boldsymbol{z}_{\text{max}} = (\frac{\sqrt{3}a_0}{2}, \frac{a_0}{2})$, $\boldsymbol{z}_{\text{sp}} = (\frac{\sqrt{3}a_0}{2}, 0)$, the points closest to the origin are chosen to simplify the calculations. We can then evaluate the sums in Eq. (3.35) to obtain:

$$\mathcal{V}^{\text{min}}_{\text{He}-\text{C}_6} = \mathcal{V}_0 + 6c_{g_1} + 6c_{g_2} \tag{3.36}$$

$$\mathcal{V}^{\text{max}}_{\text{He}-\text{C}_6} = \mathcal{V}_0 - 3c_{g_1} + 6c_{g_2} \tag{3.37}$$

$$\mathcal{V}^{\text{sp}}_{\text{He}-\text{C}_6} = \mathcal{V}_0 - 2c_{g_1} - 2c_{g_2}. \tag{3.38}$$

Subtracting $\mathcal{V}^{\text{min}}_{\text{He}-\text{C}_6}$ from $\mathcal{V}^{\text{max}}_{\text{He}-\text{C}_6}$ and $\mathcal{V}^{\text{sp}}_{\text{He}-\text{C}_6}$ will eliminate $\mathcal{V}_0$, then the system of two equations and two unknowns can be solved to give:

$$\begin{aligned} c_{g_1} &= -\frac{1}{9}(\mathcal{V}^{\text{max}}_{\text{He}-\text{C}_6} - \mathcal{V}^{\text{min}}_{\text{He}-\text{C}_6}), \\ c_{g_2} &= \frac{1}{8}\big(\mathcal{V}^{\text{sp}}_{\text{He}-\text{C}_6} - \mathcal{V}^{\text{min}}_{\text{He}-\text{C}_6}\big) - \frac{1}{9}\big(\mathcal{V}^{\text{max}}_{\text{He}-\text{C}_6} - \mathcal{V}^{\text{min}}_{\text{He}-\text{C}_6}\big)\,. \end{aligned} \tag{3.39}$$

The calculation of the hopping parameter t then proceeds as in the previous

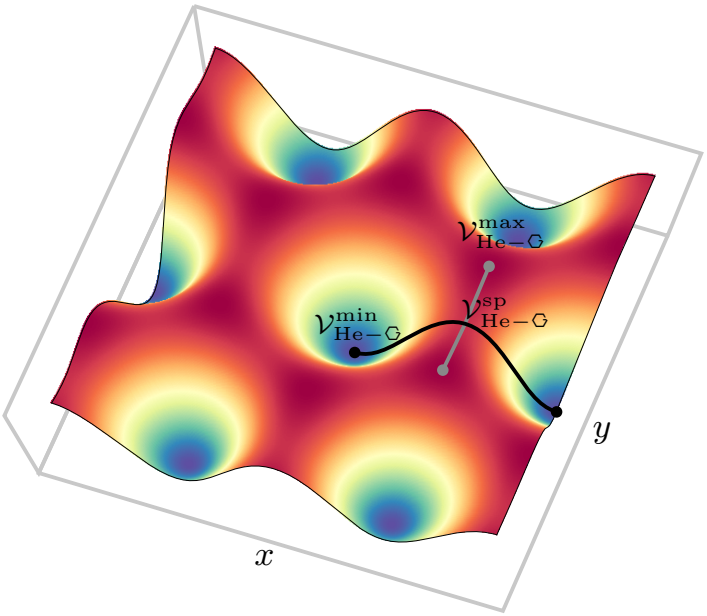

Figure 3.6: The effective 2D potential $\mathcal{V}_{\mathrm{He-G}}(x, y)$ used to calculate the hopping t can be reconstructed from MP2 and DFT calculations by determining three values corresponding to the minimum, maximum, and saddle-point values as indicated. The resulting scale along the black line can be seen in Fig. **??**.

section, where the Wannier functions are determined using the 2D potential in Eq. (3.35), leading to:

$$t_{\mathrm{DFT}} = 1.10\,\mathrm{K},\ t_{\mathrm{MP2}} = 0.59\,\mathrm{K}\,. \tag{3.40}$$

The results for t from the QMC, and DFT adsorption potentials are remarkably similar given the variation in their underlying approximations to the full 3D system. MP2, on the other hand, predicts a smaller value of t, as a result of the significantly stronger adsorption potential $\mathcal{V}_{\mathrm{He-G}}(z)$ from this method.

A summary of the relevant parameters calculated with different methods is presented in Table 3.1.

As a final check on the physical realism of these results, the WKB method can be used to estimate t as discussed in Appendix C of [1], leading to results which are in very reasonable agreement with those presented above.

Method	$\left(\mathcal{V}^{\max}_{\text{He}-\text{C}} - \mathcal{V}^{\min}_{\text{He}-\text{C}}\right)$ / (K)	$\left(\mathcal{V}^{\text{sp}}_{\text{He}-\text{C}} - \mathcal{V}^{\min}_{\text{He}-\text{C}}\right)$ / (K)
HF	21.2	17.5
QMC	24.7	21.7
DFT	39.2	36.1
MP2	72.2	66.0

Table 3.1: The parameters taken from the adsorption potential for the four different methods at the high symmetry points corresponding to the minima, maxima, and saddle point required to calculate the coefficients $c_{g_{1,2}}$ in Eq. (3.35) (HF and Wanner use the same potential).

3.3 Interaction Effects: Breakdown of the Wannier Theory

So far, we have been considering the mapping of the 2D adsorbed ^{4}He layer within the single particle approximation. Now, we proceed with an evaluation of the interaction parameters U, V, V'. In any parameterization of the He–He interaction potential, the existence of a strong hard-core will preclude the double occupation of a single site on the triangular lattice and thus effectively $U = \infty$ as it is the dominant scale with $U \gg t, V, V'$. For the potentials in Fig. 3.13(a) we find that Eq. (3.8) yields $U > 10^6\,\text{K}$. Therefore, the effective Bose–Hubbard model describes hard-core bosons hopping on the triangular lattice formed by the graphene hexagon centers (Fig. 1.2). Using the single-particle Wannier function approach, one can also compute the nearest neighbor (V) and next-nearest neighbor (V') parameters directly from Eqs. (3.9) and (3.10) which lead to

$$V_{\text{W}} = 7540\,\text{K},\ V'_{\text{W}} = 638\,\text{K}. \tag{3.41}$$

The resulting enormous energy scales associated with these parameters are unphysical and suggest that the spatial extent of one-particle wave function is

too large, and fails to capture the correct interaction physics. This catastrophe originates from the fact that we study the adsorption of ^{4}He atoms on a solid-state substrate and consequently both the spatial extent of the one-particle wavefunction (determined by the graphene lattice structure), and the most prominent (repulsive) part of the He–He potential, vary on the same length scale, of order of several Å.

This is in contrast to the case of dilute cold atomic gases confined in optical lattices, where the confinement scale, as well the optical lattice wavelength ("lattice spacing"), are typically on the order of a µm. These scales are much larger than the range of the interaction potential ($\sim 10\,\text{Å}$) such that the two-body interaction is contact-like and is assumed to be described by a δ-function.

Thus in cold atom systems, which provide the main examples of Bose–Hubbard models and associated quantum phase transitions in nature, the one-body confinement scale and the two-body interaction scale are well separated. Due to this, the effective model is of the $t-U$ type [66], with a finite Hubbard U and irrelevant (i.e. much smaller) additional interactions V, V'.

In the case where the 2D limit is reached via adsorption on graphene, the very strong He–He repulsion on the scale of the one-particle wave-function effectively produces an infinite on-site Hubbard U and therefore it is the nearest-neighbor V and next-nearest neighbor V' that determine the relevant quantum phases of the system, leading to the hard-core $t-V-V'$ model considered here. Therefore, the determination of V, V' presents considerable technical challenges and has to be done via sophisticated techniques that take into account the correct structure of the wave function which is modified by two-body interactions and at finite density deviates significantly from the one-particle results presented so far. In this sense, our analysis is quite unconventional compared to the usual approaches to the Bose–Hubbard model. Because of the well-localized

structure of the many-body wave functions (as will be clear from the results of the next sections), the effective Bose–Hubbard model is still dominated by two-body (density–density) interactions, with the nearest-neighbor term being the largest one ($V \gg |V'|$).

The remainder of this section presents a number of different approaches to gain access to the many-body wavefunctions of ^{4}He on graphene in order to compute V and V' exemplifying the strong correlations in the problem.

3.4 Hartree–Fock Approach to Interaction Parameters

Here we provide details on how the parameters V and V' of the effective Bose–Hubbard model can be computed from an effective 2D model of the adsorbed layer. Since V is the energy of nearest-neighbor interaction, then for its computation, one needs to consider a helium layer with a unit filling fraction. However, as noted in § 2.1, ^{4}He atoms at this density form two, not one, layers on top of graphene. To resolve this issue, we will rely on an important result from our QMC simulations, which is described in detail in § 3.5. Namely, a quasi-2D, single-layer arrangement of helium over graphene is restored when one imposes a confining potential in the z-direction. Importantly, the particle density in that direction obtained with the confinement is close to the density profile at filling fraction $f = 1/3$; see e.g. Figs. 3.10 and 3.11. This justifies the use of a 2D model for the approximate computation of nearest-neighbor He–He interactions.

Let us stress again that the spatial extent of the maximally localized Wannier functions found in the previous subsection (well-suited for the description of an isolated helium atom), is on the order of the spacing between the near-

est graphene hexagon centers. Therefore, the standard approach of computing interaction parameters in the Bose–Hubbard model via the overlap integral Eq. (3.9) would give an unphysically large result. However, we note that the mutual repulsion of adjacent helium atoms narrows their wavefunctions considerably compared to the Wannier functions (see Fig. 3.5). We will now show how these narrower wavefunctions are found and then use them in the calculation of V and V' via Eqs. (3.9) and (3.10).

Such wavefunctions are obtained by numerically solving a system of 2D Hartree–Fock equations [38]:

$$-\frac{\hbar^2}{2m}\nabla_{\boldsymbol{\rho}}^2\psi_i(\boldsymbol{\rho}) + \mathcal{V}_{\mathrm{He-C}}(\boldsymbol{\rho})\psi_i(\boldsymbol{\rho}) + \sum_{i\neq j}\int \mathrm{d}\boldsymbol{\rho}'\ \psi_j^*(\boldsymbol{\rho}')\mathcal{V}_{\mathrm{He-He}}(\boldsymbol{\rho}-\boldsymbol{\rho}')\times[\psi_j(\boldsymbol{\rho}')\psi_i(\boldsymbol{\rho}) + \psi_i(\boldsymbol{\rho}')\psi_j(\boldsymbol{\rho})] = \tilde{E}_i\psi_i(\boldsymbol{\rho})\,, \quad (3.42)$$

where the wavefunctions $\psi_i(\boldsymbol{\rho}) \equiv \psi(\boldsymbol{\rho}-\boldsymbol{\rho}_i)$ also satisfy the orthonormality constraint:

$$\int \mathrm{d}\boldsymbol{\rho}\psi_i(\boldsymbol{\rho})\psi_j(\boldsymbol{\rho}) = \delta_{ij}\,, \quad (3.43)$$

with δ_{ij} being the Kronecker delta.

Equations (3.42) and (3.43) were solved by the accelerated imaginary-time evolution method (a variant of fixed-point iterations), whose general framework for systems of equations subject to constraints were laid out in [71]; its technical details will be described elsewhere. To estimate the significance of the exchange interaction (i.e., the last term, $\psi_i(\boldsymbol{\rho}')\psi_j(\boldsymbol{\rho})$, in Eq. (3.42)), we also simulated the Hartree approximation, obtained from Eq. (3.42) by dropping that term and not imposing the constraint in Eq. (3.43).

We performed simulations for the z-averaged potentials $\mathcal{V}_{\mathrm{He-C}}$ and $\mathcal{V}_{\mathrm{He-He}}$, as described in Appendix A of [1]. For the potentials averaged with two different $\rho(z)$'s: that defined in Appendix A of [1] and that found by QMC (§ 3.5),

Eq. (3.9) gives, respectively: $V_{\rm HF} = 69.7$ and 62.2 K. The reason for the latter value being smaller is that $\mathcal{V}_{\rm He-He}$ is reduced (smoothened) more by the more spread-out $\rho(z)$ obtained by the QMC. On the other hand, the contribution of the difference between the two averaged $\mathcal{V}_{\rm He-\bigcirc}$'s to the difference in the corresponding V's is negligible. In fact, we found that the effect of even larger — on the order of 50% — changes in the magnitude of $\mathcal{V}_{\rm He-\bigcirc}$ on V was well under 1%. For completeness, we also note that when we used $\mathcal{V}_{\rm He-\bigcirc}$ and $\mathcal{V}_{\rm He-He}$ averaged with $\rho(z)$ defined in Appendix A of [1] but used the Hartree rather than Hartree–Fock approximation, we found $V = 72.4$ K. Finally, the parameter V' computed from Eq. (3.10) by any of these approximations equals -2.1 K to two significant figures. (The number quoted in Table 1.1 is for the first aforementioned case.)

We conclude that the Hartree–Fock method leads to remarkably strong downward renormalization with respect to the one-particle (Wannier theory) result Eq. (3.41). To summarize, the interaction parameters computed by the Hartree–Fock approximation are:

$$V_{\rm HF} = 69.7\,{\rm K},\ V'_{\rm HF} = -2.08\,{\rm K}. \tag{3.44}$$

For a system of localized bosons with strong short-range interactions, the Hartree–Fock equations provide a very accurate description as many-particle correlations beyond the scope of the method are expected to be weak. In addition, and quite reassuringly, we find that the above results are similar to those obtained by the accurate many-body quantum Monte Carlo technique.

3.5 Quantum Monte Carlo

At $T = 0\,\mathrm{K}$, the path integral ground state quantum Monte Carlo (QMC) algorithm [72, 73, 74] provides access to ground state properties of a many-body system by statistically sampling the imaginary time propagator $e^{-\beta H}$. Starting from a trial wave function $|\Psi_\mathrm{T}\rangle$, in the long imaginary time limit $\beta \to \infty$, $e^{-\beta H}\,|\Psi_\mathrm{T}\rangle$ converges to the exact ground state, $|\Psi_0\rangle$, provided $\langle\Psi_0|\Psi_\mathrm{T}\rangle \neq 0$. Within this framework we can directly compute ground state properties by statistically sampling the expectation value of an observable $\mathcal{O}$, via:

$$\langle\mathcal{O}\rangle \simeq \frac{\langle\Psi_T|\mathrm{e}^{-\beta H}\mathcal{O}\mathrm{e}^{-\beta H}|\Psi_T\rangle}{\langle\Psi_T|\mathrm{e}^{-2\beta H}|\Psi_T\rangle}. \tag{3.45}$$

We work in a first-quantized representation $|\boldsymbol{R}\rangle$ in 3 spatial dimensions where configurations are sampled from the 3+1 dimensional imaginary time worldlines of interacting particles. Appendix B of [1] provides additional details on the convergence and scaling of our QMC approach and the source code can be found online [75].

In the remainder of this subsection we discuss how QMC simulations of the 3D microscopic many-body Hamiltonian in Eq. (1.3) can be analyzed in the context of an emergent 2D Bose–Hubbard model. We begin by confirming the single-particle description of the adsorbed monolayer described in Section 2.1 which allows us to compute an effective 2D potential that can be used to determine the hopping parameters t. We then proceed by reducing the size of the simulation cell in the z-direction where the extra dimensional confinement allows us to stabilize a monolayer at the large filling fractions needed to determine the interaction parameters V and V'.

3.5.1 Single Particle Properties: $f = 1/N_{\hexagon}$

We begin with the simplest case of considering a single ^{4}He atom proximate to the graphene surface at $T = 0$. The results of QMC simulations are shown in Figure 3.7 for $N = 1$ with $N_{\hexagon} = 24$ adsorption sites that are commensurate in a cell with volume $L_x \times L_y \times L_z = 9.84\,\text{Å} \times 12.78\,\text{Å} \times 10.0\,\text{Å} = 1257\,\text{Å}^3$. The cell has periodic boundary conditions in the x and y directions, while motion in the z-direction is restricted through the graphene sheet at $z = 0$ and a hard wall at $z = L_z$ enforced by the potential

$$\mathcal{V}_{\text{wall}}(z) = \frac{\mathcal{V}_{\text{He}-\hexagon}(\boldsymbol{r}_{\text{min}})}{1 + \text{e}^{(L_z - r_{\text{vdW}} - z))/\Delta}}. \tag{3.46}$$

Here, $\boldsymbol{r}_{\text{min}} = a_0(\sqrt{3}/2, 1/2, 1)$ is located at $z = a_0$ above a carbon atom such that $\mathcal{V}_{\text{He}-\hexagon}(\boldsymbol{r}_{\text{min}}) \sim \text{O}(10^5)$ K sets the scale of the repulsive potential, $r_{\text{vdW}} \approx 1.4\,\text{Å}$ is the van der Waals radius of helium, while $\Delta = 0.05\,\text{Å}$ defines the rapidness of its onset. The functional form of Eq. (3.46) and the choice of parameters are unimportant at filling fractions $f \lesssim 1/2$ provided $L_z \gtrsim 6\,\text{Å}$. For the value $L_z = 10\,\text{Å}$ considered here, simulation results are independent of L_z and can be considered to be reflective of bulk adsorption phenomena.

Figure 3.7(a) shows the particle density in the z-direction determined from the expectation value $\rho(z) = \left\langle \sum_{i=1}^{N} \delta(z_i - z) \right\rangle \propto \iint \text{d}x\,\text{d}y\,|\Psi_0(x, y, z)|^2$ via Eq. (3.45) ($N = 1$ here). It has a well-defined peak near 2.7 Å and a corresponding sub-Å width (shown as the full width half maximum) demonstrating that adsorbed ^{4}He atoms indeed form a quasi-two dimensional layer. Panel (b) includes the average particle density in the plane normalized such that $N = \iint \text{d}x\,\text{d}y\,\rho(x, y)$ and the existence of density in each of the $N_{\hexagon} = 24$ adsorption sites is evidence of particle hopping and an ergodic simulation. The lower panel (d) is a cut showing the scale of density fluctuations. Panel (c)

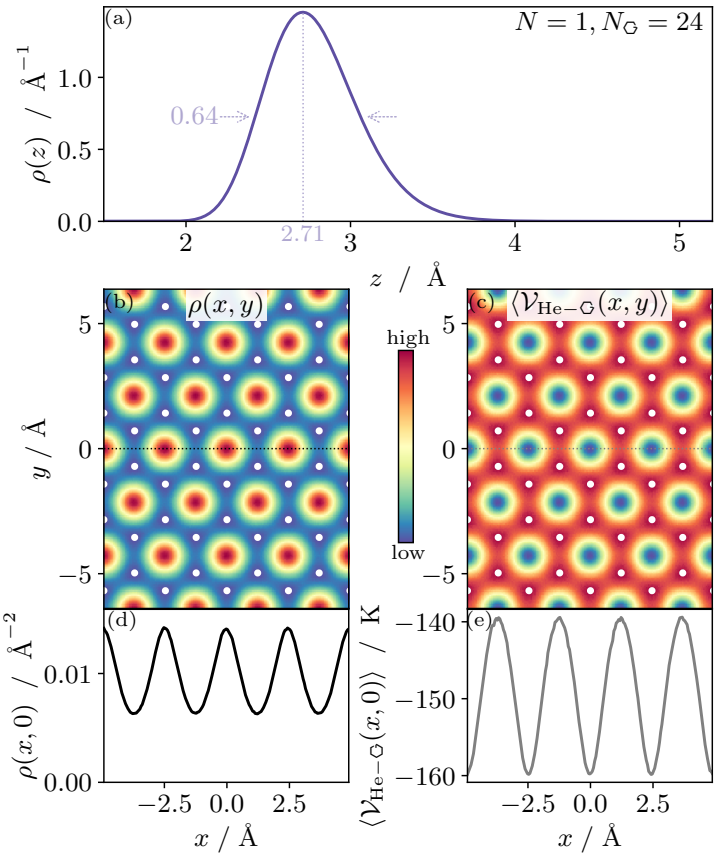

Figure 3.7: Quantum Monte Carlo results for a single ^{4}He atom ($N = 1$) above a graphene membrane with $N_{\mathrm{G}} = 24$ adsorption sites. (a) The average density in the z-direction showing a well defined particle position a distance 2.71 Å above the sheet with a width of 0.64 Å. (b) The average density in the xy-plane showing the ability of a single particle to *hop* between the sites of the triangular lattice. White dots show the location of carbon atoms (not to scale). (c) The average potential energy experienced by the ^{4}He atom due to the graphene sheet in the xy-plane. (d) A horizontal cut of the particle density $\rho(x, y)$ along the line $y = 0$. (e) A horizontal cut of the adsorption potential $\mathcal{V}_{\mathrm{He-G}}(x, y)$ along the line $y = 0$.

shows the average adsorption potential experienced by the ^{4}He as it moves in 2D:

$$\langle \mathcal{V}_{\text{He}-\text{G}}(x,y)\rangle \equiv \left\langle \frac{\int \mathrm{d}z\, \mathcal{V}_{\text{He}-\text{G}}(x,y,z)\rho(x,y,z)}{\int \mathrm{d}z\, \rho(x,y,z)} \right\rangle \tag{3.47}$$

while (e) is a horizontal cut along the line $y = 0$ highlighting that the minimum-to-saddle corrugation is $\mathcal{V}^{\text{sp}}_{\text{He}-\text{G}} - \mathcal{V}^{\text{min}}_{\text{He}-\text{G}} \simeq 20.5\,\text{K}$ (on the order of the kinetic energy). The trough-to-maximum depth of the adsorption potential is $\mathcal{V}^{\text{sp}}_{\text{He}-\text{G}} - \mathcal{V}^{\text{min}}_{\text{He}-\text{G}} \simeq 23.6\,\text{K}$. These values are reduced by approximately 25% with respect to the bare potential in Eq. (1.4) integrated over the wavefunction in panel (a). This softening is due to the spatial extent in the z-direction and partial localization of the wavefunction in the xy-plane.

These QMC results for a single particle can be used in conjunction with the band structure analysis introduced in § 3.2 to map the system to a non-interacting Bose–Hubbard model. In particular, under the assumption that an adsorbed ^{4}He atom is confined in a 2D layer, we employed $\langle \mathcal{V}_{\text{He}-\text{G}}(x,y)\rangle$ and extracted t from the resulting spectrum in Fig. 3.4. This is equivalent in principle to using the overlap in Eq. (3.7) for a real wavefunction $|\Psi_\perp(x,y)|^2 \propto \rho(x,y)$ where the QMC average has been performed by exploiting translational invariance, i.e. moving from the Bloch to Wannier basis. The resulting localized single particle wavefunction (labelled QMC) was previously shown in Fig. 3.5. We find:

$$t_{\text{QMC}} = 1.38(1)\,\text{K}\,.$$

3.5.2 Many-Body Adsorption: $f > 0$

In order to investigate the effects of He–He interactions and thus determine the effective parameters V and V' in the Bose–Hubbard model we need to increase the filling fraction until ^{4}He atoms occupy every site of the triangular lattice defined by hexagon centers. However, as discussed in § 2.1, as the density of

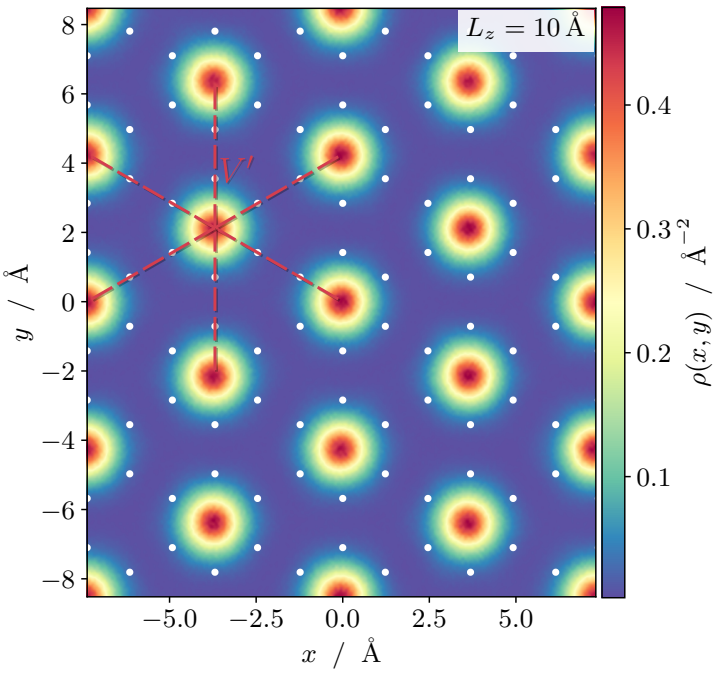

Figure 3.8: The two-dimensional density of particles $\rho(x, y)$ obtained from ground state quantum Monte Carlo simulations for a simulation cell with $L_x \times L_y \times L_z = 14.75707 \times 17.04 \times 10.0$ Å corresponding to the C1/3 phase with $f = 1/3$ for $N = 16$ ^{4}He atoms on $N_{\hexagon} = 48$ adsorption sites. Finite size effects in the spatial wavefunction are negligible beyond $N_{\hexagon} = 12$.

helium atoms near the surface is increased, the strong repulsive interaction in Eq. (1.3) will cause layer completion and promote the growth of further layers such that the system can no longer be considered within the 2D approximation.

It is thus easier to first consider the case of $f = 1/3$ where a commensurate (so-called C1/3) solid phase is stable over a range of chemical potentials. Performing a quantum Monte Carlo simulation for a system with $N = 16$ particles near $N_{\hexagon} = 48$ adsorption sites yields the 2D density profile $\rho(x, y)$ shown in Fig. 3.8. Note that in contrast to Fig. 3.7(b) for $f = 1/N_{\hexagon}$, here the local spread of the wavefunction around the hexagon centers in the xy-plane is strongly reduced with vanishing density between. The ground state is a stable solid and interactions are mediated through next-nearest neighbor sites at a distance of $3a_0$ as indicated with dashed lines in analogy with Fig. 1.2. In order

to estimate the value of V' from this data, we can compute the ground state energy in the 2D Bose–Hubbard model in Eq. (1.2) for a Fock state characterizing the C1/3 phase, denoted by $|\hexagon\rangle$, where the kinetic energy and nearest neighbor interaction terms are identically zero:

$$\langle\hexagon|H_{\mathrm{BH}}|\hexagon\rangle \equiv E_{\mathrm{BH}}\Big|_{f=1/3} = 3NV' = N_{\hexagon}V' \,, \tag{3.48}$$

where we are neglecting the effects of even further V'' interaction terms. Thus, measuring the total contribution of the interaction potential to the ground state energy in QMC, $\langle\mathcal{V}_{\mathrm{He-He}}\rangle$ and equating this with E_{BH}, we identify:

$$V'_{\mathrm{QMC}} = \frac{1}{N_{\hexagon}} \langle\mathcal{V}_{\mathrm{He-He}}\rangle_{f=1/3} \tag{3.49}$$

and estimate:

$$V'_{\mathrm{QMC}} = -2.76(2)\,\mathrm{K}$$

from the finite size scaling analysis described in Appendix B of [1]. This value differs by 25% from a naive estimate computed from the bare He–He interaction: $V'_{\mathrm{He-He}} = \mathcal{V}_{\mathrm{He-He}}(|\boldsymbol{r}| = 3a_0) \simeq -2.0\,\mathrm{K}$.

In order to perform a similar procedure to extract V, we need to hinder the formation of multiple layers which can be accomplished by restricting our simulation cell in the z-direction using (3.46). However, it is not clear which value of L_z will (1) maintain the existence of a single well-defined 2D monolayer as the filling is increased past $f \simeq 0.6$ and (2) not significantly modify the behavior near filling fraction $f = 1/3$ where the equation of state shows a minimum. The latter is especially important as the behavior of the 2D Bose–Hubbard model is well understood in this regime [49, 50, 51]. In order to answer these questions, we have performed QMC simulations at filling fractions: $f = 1/3, 1$ for $L_z \in [4.5, 5.5]$ and $N_{\hexagon} = 24, 48, 96$. Finite size effects in $N_{\hexagon}$ were

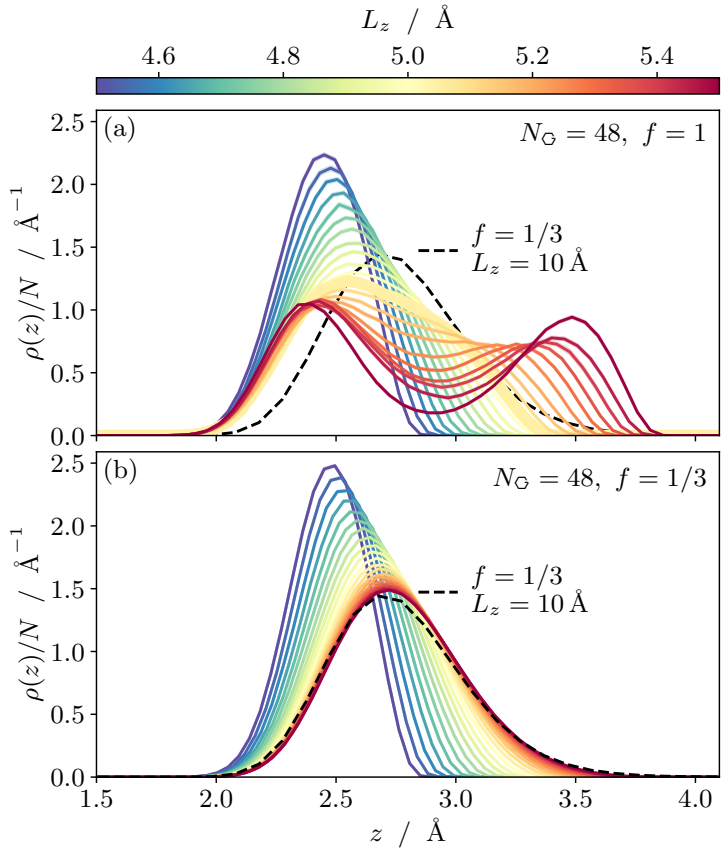

Figure 3.9: The density profile (per particle) of the adsorbed layer(s) for different vertical box sizes L_z enforced through the potential in Eq. (3.46) for helium above a graphene sheet with $N_{\mathrm{G}} = 48$ adsorption sites such that $L_x \times L_y = 14.757\,07\,\text{Å} \times 17.04\,\text{Å}$. Panels correspond to (a) filling $f = 1$ and (b) $f = 1/3$ where statistical uncertainties are indicated by the shaded envelope. The thicker curve in (a) for $L_z = 5.05\,\text{Å}$ was determined to be the optimal value (see text). The dashed line indicates the density profile for a "bulk" cell with $L_z = 10\,\text{Å}$ at $f = 1/3$ that is used for comparison. The number of ^{4}He atoms in the simulation can be determined from $N = fN_{\mathrm{G}}$.

negligible for the density profiles in the z-direction, and we show simulation results for $N_{\hexagon} = 48$ in Fig. 3.9. Here panels correspond to different filling fractions and colors to different values of L_z.

In panel (a) at unit filling ($f = 1$) we observe that the density $\rho(z)$ smoothly evolves as a function of L_z from one that contains a single well-defined layer for small box sizes ($L_z \lesssim 5\,\text{Å}$), to a profile with two peaks in the density for $L_z \gtrsim 5\,\text{Å}$. In order to quantify these two regimes and determine at which value of L_z we should analyze the system, we performed additional simulations at $f = 1/3$ (Fig. 3.9(b)) where we observe less drastic effects of the confinement. At this lower filling, results are clearly approaching the bulk case for $f = 1/3$ with $L_z = 10\,\text{Å}$ beyond $L_z \gtrsim 5.5\,\text{Å}$ as indicated by the dashed line. This data can then be exploited by searching for the value of L_z at unit filling that produces a density profile most similar to that of the bulk monolayer at $f = 1/3$ within the approximation that interactions in the plane should not seriously affect the z-spread of the wavefunction. To proceed, we search for a minimum in the squared deviation of densities:

$$\chi^2(L_z) \equiv \sum_i \left[\frac{\rho(z_i)}{N_{\hexagon}}\bigg|_{\substack{L_z \\ f=1}} - \frac{\rho(z_i)}{N_{\hexagon}/3}\bigg|_{\substack{Lz=10\,\text{Å} \\ f=1/3}} \right]^2 \tag{3.50}$$

where i runs over all spatial positions in z where density data has been obtained. The results of this procedure are shown in Fig. 3.10 and indicate a quadratic dependence on L_z with the minimum occurring at $L_z = 5.05\,\text{Å}$. At this value of L_z, the inset shows a comparison of the two density profiles from Fig. 3.9. Finite size effects in $N_{\hexagon}$ were not found to alter the optimal value of L_z.

Recall that the goal of this procedure was to stabilize a single monolayer at filling fraction $f = 1$ in order to determine the effects of nearest and next-nearest neighbor interactions between ^{4}He atoms without substantially distorting the

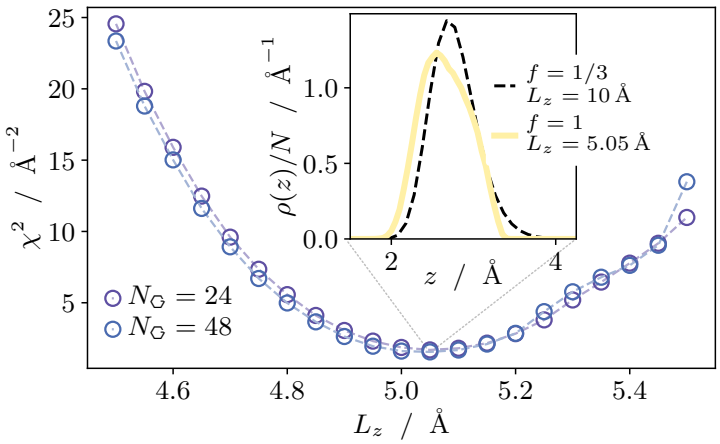

Figure 3.10: The squared deviation between solid and dashed curves in Fig. 3.9(a) as a function the box size in the z-direction as quantified in Eq. (3.50). The minimum at $L_z = 5.05\,\text{Å}$ is independent of the size of the graphene sheet, where data for $N_{\text{G}} = 24$ and 48 are shown. The inset shows a comparison of the density profiles in the z-direction for this value at $N_{\text{G}} = 48$. The dashed line is a guide to the eye.

physics of the adsorbed phase. As an additional check, we have computed the equation of state at $L_z = 5.05\,\text{Å}$ and compared it with that determined for the unrestricted bulk cell with $L_z = 10\,\text{Å}$ for a system with $N_{\text{G}} = 24$ adsorption sites. The results, shown in Fig. 3.11, demonstrate that the additional confinement potential in Eq. (3.46) does not alter the ground state properties of the adsorbed monolayer for $f \lesssim 0.6$. The insets show that the monolayer profile remains mostly unchanged for filling fraction $f = 1/3$. At unit filling with $f = 1$, while the confined box with $L_z = 5.05\,\text{Å}$ still exhibits only a single layer, the unbounded cell can now accommodate an energetically favorable second layer.

Thus, provided we are interested in constructing a low energy effective model at lower filling for a monolayer, we conclude that $L_z = 5.05\,\text{Å}$ is an appropriate choice for simulations at $f = 1$. In this case, the ground state is an insulator as seen in the 2D density in Fig. 3.12. Here, the wavefunction is strongly localized near the center of a graphene hexagon, with a cut along $y = 0$ having been previously shown in Fig. 3.5. Following similar logic to that employed for the

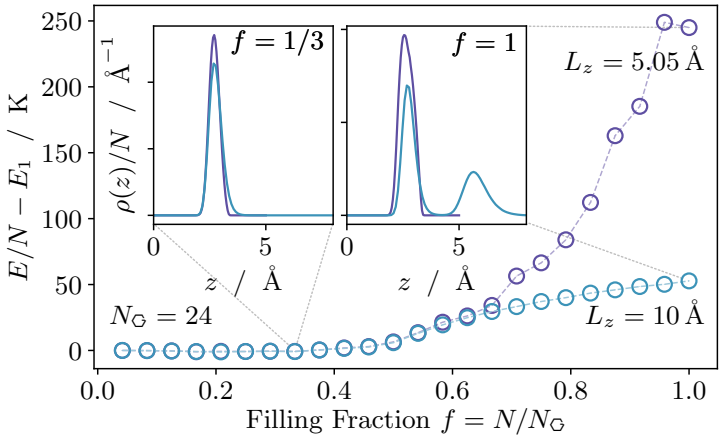

Figure 3.11: Equation of state (energy per particle as a function of filling fraction) for $N_{\mathrm{G}} = 24$ adsorption sites for two box sizes with $L_z = 5.05, 10.0$ Å. The curves have been shifted by the energy for a single particle $N = 1$ corresponding to a filling fraction-independent value of ~ 6 K due to the presence of $\mathcal{V}_{\mathrm{wall}}$. The insets show the density of particles along the z-direction at filling fractions $f = 1/3$ and 1. For unit filling, the cell with $L_z = 10$ Å can accommodate a second layer.

insulating phase at $f = 1/3$, Eq. (3.49), we examine the Bose–Hubbard model on the triangular lattice at $f = 1$ where $\langle \triangle | H_{\mathrm{BH}} | \triangle \rangle \equiv E_{\mathrm{BH}}\big|_{f=1} = 3VN + V'N$ and compute

$$V_{\mathrm{QMC}} = \frac{1}{3N} \langle \mathcal{V}_{\mathrm{He-He}} \rangle_{f=1} - V'_{\mathrm{QMC}}. \tag{3.51}$$

The results are shown in Fig. 3.13 as a function of L_z and we identify:

$$V_{\mathrm{QMC}} = 54.3(1)\,\mathrm{K}$$

at $L_z = 5.05$ Å, where the uncertainty in the last digit arises from a combination of stochastic errors and finite size effects. This value is larger than an estimate obtained from the bare interaction potential for two helium atoms separated by the nearest-neighbor distance: $V_{\mathrm{He-He}} = \mathcal{V}_{\mathrm{He-He}}\big(|\boldsymbol{r}| = \sqrt{3}a_0\big) \simeq 31$ K. While there are very limited finite size effects in N_{G}, the chosen value of L_z does have an effect on the value of V_{QMC}, reducing it from 61.5 K at $L_z = 4.5$ Å to 49.0 K

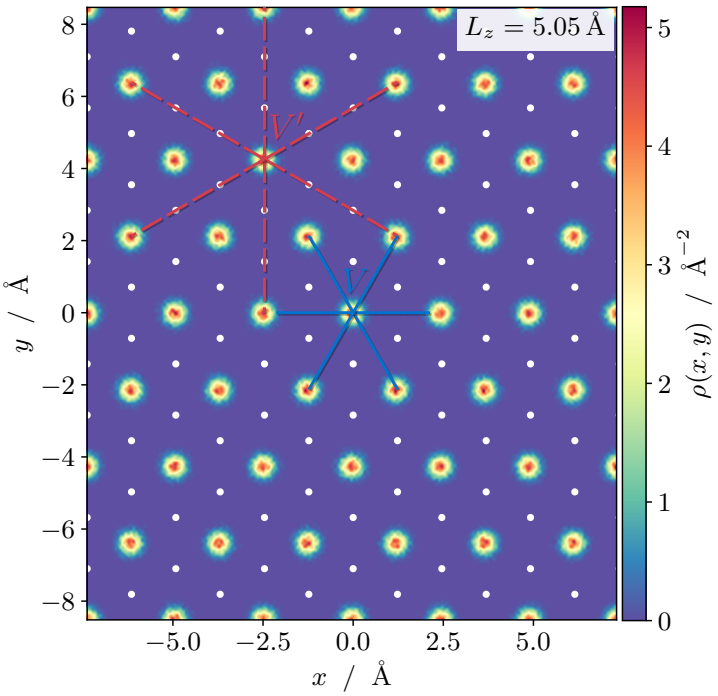

Figure 3.12: The two-dimensional density of particles $\rho(x, y)$ obtained from ground state quantum Monte Carlo simulations for a simulation cell with $L_x \times L_y \times L_z = 14.75707 \times 17.04 \times 5.05$ Å corresponding to the fully filled phase with $f = 1$ for $N = 48$ ^{4}He atoms on $N_{⬡} = 48$ adsorption sites. Finite size effects in the spatial wavefunction are negligible beyond $N_{⬡} = 12$. Nearest neighbor (V) and next-nearest neighbor (V') couplings in the effective Bose–Hubbard description are indicated with solid and dashed lines, respectively.

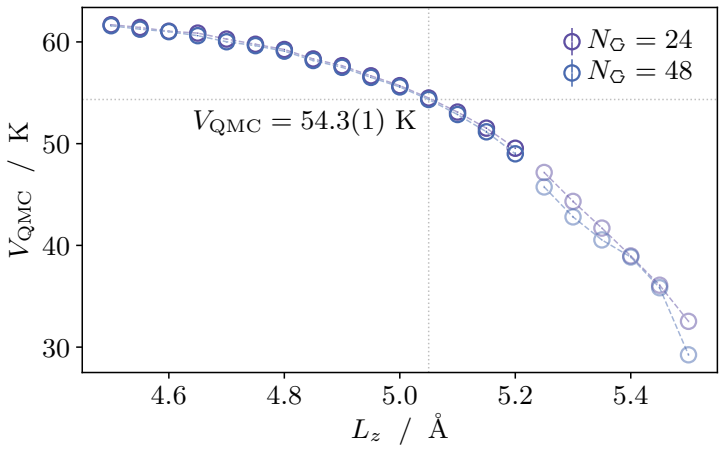

Figure 3.13: The effective nearest neighbor interaction parameter of the Bose–Hubbard model computed from Eq. (3.51) via quantum Monte Carlo for simulation cells with $N_{\mathrm{G}} = 24, 48$ as a function of the cell size in the z-direction, L_z. The indicated value of $V_{\mathrm{QMC}} = 54.3(1)\,\mathrm{K}$ was computed at $L_z = 5.05\,\text{Å}$ as described in the text. The semi-transparent symbols for $L_z \geq 5.25\,\text{Å}$ indicate cell sizes which allowed the nascent formation of a second layer, where the mapping of the microscopic Hamiltonian to the 2D Bose–Hubbard model breaks down.

at $L_z = 5.2\,\text{Å}$. For larger values of L_z, there is no longer a single well-defined monolayer and the rapid reduction in V observed in Fig. 3.13 can be attributed to the promotion of a second layer where ^{4}He atoms can now move to larger values of z to minimize their repulsive interaction (as seen in Fig. 3.9).

Chapter 4

Ab initio Calculations of V

This chapter contains sections and figures quoted verbatim from the following published work by the author [1], mainly consisting of work done by the co-authors of that work. The author's contributions is extracting the potential at the high-symmetry points and calculating the hopping t for the methods of this chapter.

4.1 Density Functional Theory

We performed DFT calculations with the PBE (Perdew–Burke–Ernzerhof) generalized gradient approximation [76] for the exchange–correlation functional and projector augmented wave (PAW) [77] pseudopotentials (PPs), as implemented in the Quantum Espresso electronic structure package [39, 40]. For He–graphene calculations, one or two He atoms are placed at a specified distance from a periodic graphene sheet consisting of 6×6 unit cells within a hexagonal simulation cell with a vacuum region of 30 Å. For He–He calculations, two He atoms are placed at a specified distance within a cubic simulation cell of 30 Å. PAW PPs for C and He were obtained from the standard solid-state PP library [78, 79, 80]. We applied the DFT-D4 semi-empirical dispersion correction

[41, 42, 43] when computing single point energies and structural optimizations to account for long-range electronic–correlation effects. The energy cut-off for wavefunctions was 50 Ry (680 eV) and 360 Ry (4900 eV) for the charge density and potential. The Brillouin zone is sampled using a Monkhorst–Pack grid with $6 \times 6 \times 1$ k-points.

To obtain the energies of the He-graphene interaction along the path that connects two neighboring minima of the potential (between centers of neighboring lattice sites and passing through the saddle point), the position of the He atom is fixed in the plane of the sheet and the optimal distance from the sheet is then found at each point to compute the energy along the minimum energy surface (see Fig. **??**). We followed the same approach to find the maximum value of he potential (centered at the position of a C atom) with the results shown in Table 3.1.

For He–He on graphene calculations, two He atoms are placed at the centers of various lattice sites and at an optimal distance from the sheet, obtained beforehand for a single He atom ($z_{\text{opt}} \simeq 3.036\,\text{Å}$, see Fig. 1.4). The resulting interaction (relative to non-interacting adsorbed atoms) provides an estimate for the nearest and next-nearest neighbor values:

$$V_{\text{DFT}} = 21.4\,\text{K} \quad V'_{\text{DFT}} = -1.36\,\text{K}. \tag{4.1}$$

4.2 Møller–Plesset Perturbation Theory

Because the He–He and He–graphene interactions are dominated by dispersion terms which require accurate treatment of the correlation energy [45, 46], second-order Møller–Plesset (MP2) [44] perturbation theory calculations, which in most cases capture ca. 95% of the correlation energy [45], were performed using Gaussian 09 [81] utilizing Pople-type [82] bases sets up to 6-31++G(d,3p),

which include diffusion of all orbitals, and polarization functions d and p for all atoms.

Such a high-order basis set was needed to obtain the He–He interactions in vacuum to reasonable accuracy (Fig. 1.4(a)). To model the interaction of He atom(s) with graphene (and possible modifications of the He–He potential on graphene), a sequence of increasing aromatic molecules was considered (benzene, coronene, hexabenzocoronene, circumcoronene — the latter with 54 C and 18 H atoms). The energy of the system was computed for different values of z between the He atom(s) and the C plane, and the asymptotic energy for $z \to \infty$ was removed as a baseline. To reproduce graphene, the aromatic molecules were constructed with C–C distances constrained to $a_0 = 1.42\,\text{Å}$, and only the coordinates of terminating H atoms were optimized. Figure 1.4(b) shows the potential energy vs. height for a single He atom above the center of a circumcoronene molecule. We observed that the calculations converge after hexabenzocoronene and there was a relatively small "radial dependence" of $\mathcal{V}_{\text{He}-\text{C}}(r, z)$ for other hexagon centers, making this a reasonable model for He on graphene.

We also performed scans of the potentials over different positions over the circumcoronene. Figure 3.6 depicts the dependence of $\mathcal{V}_{\text{He}-\text{C}}(x, y, z_0)$, i.e., the lateral dependence of the He–graphene minimum energy surface (values in Table 3.1) which allows for the calculation of t_{MP2} reported in §3.2.

Additionally, we performed calculations for the energy for two He atoms adsorbed onto various hexagon centers. After removing the baseline $2 \times \mathcal{V}_{\text{He}-\text{C}}$ terms, we find a remnant $\mathcal{V}_{\text{He}_\text{C}-\text{He}_\text{C}}(r)$ which remains strongly repulsive for nearest neighbors ($r = 2.46$ Å) and attractive for next-nearest neighbors and beyond ($r \geq 4.26$ Å):

$$V_{\text{MP2}} = 51.5\,\text{K}, \quad V'_{\text{MP2}} = -1.97\,\text{K}\,. \tag{4.2}$$

Chapter 5

Conclusions and Future Work

5.1 Discussion

Our main result is the construction of a reliable and consistent description of the effective two-dimensional adsorption problem of helium-4 on graphene using the hard-core Bose–Hubbard Model, Eq. (1.2). The hopping and interaction parameters computed via different techniques are summarized in Table 5.1. The differences in the hopping and interaction parameters can be intuitively understood by examining Fig. 1.4. The variation in t can be explained by the depths of the adsorption potential $\mathcal{V}_{\mathrm{He-C}}$. A stronger adsorption potential leads to a more localized waverfunction, which means hopping is less likely. Correspondingly, we can see that the method with the deepest adsorption potential, MP2, has the smallest t while the shallowest empirical potential produces the largest t. The variation in V can be explained by the strength of the He-He interaction $\mathcal{V}_{\mathrm{He-He}}$ for each method. At the distance of one lattice spacing, the empirical and MP2 potentials are strongly repulsive and corresponds to the largest V, while the DFT potential is slightly attractice, leading to the smallest V.

Regardless of the small variations in the parameters calculated via each method, aside from the pure Wannier calculations, places the system of He

Method	t / (K)	V / (K)	V' / (K)	t/V
Wannier	1.45	7540	638	0.0002
HF	1.45	69.7	-2.08	0.021
QMC	1.38	54.3(1)	-2.76(2)	0.025
DFT	1.10	21.4	-1.36	0.051
MP2	0.59	51.5	-1.97	0.011

Table 5.1: The hopping parameter t, nearest and next nearest-neighbor interaction V and V', and the ratio of t/V of the effective Bose–Hubbard model defined in Eq. (1.2) as calculated by the five different methods: Wannier functions, Hartree–Fock (HF), quantum Monte Carlo (QMC), Density Functional Theory (DFT), and Møller–Plesset perturbation theory (MP2). In all cases, t is calculated via the band structure of single helium atom subject to a periodic two-dimensional adsorption potential $\mathcal{V}_{\text{He}-\text{G}}$. Note that t is the same for Wannier and Hartree–Fock as they use the same empirical potential.

adsorbed graphene deep in the commensurate 1/3 filling phase, as show in Fig.5.1. It is clear that the first layer of He adsorbed on graphene is unlikely to be a superfluid. This is not suprising considering the decrease in adsorption potential from graphite to graphene, 10%, is much less than the decrease in adsorption potential from the first layer to the second layer, about 80%, regardless our experience with constructing this Bose–Hubbard model has given us some unique insights. Unlike the usual examples of BH models that involve cold atoms, where the lengths scale of the lattice is far larger than the lengths scale of the particle-particle interactions, the He-He interactions are significant at the lengths scale of the lattice. This means that special attention had to be payed to the He-He interactions in order to produce accurate results. It is hoped that this unique case of a Bose–Hubbard model construction can prove enlightening.

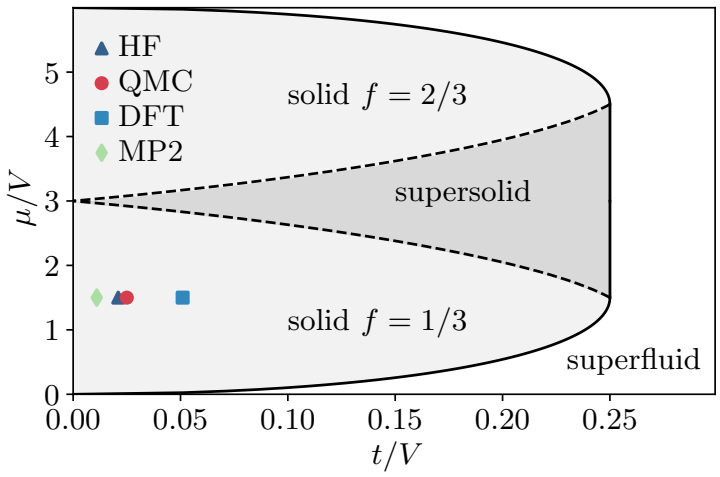

Figure 5.1: The mean-field phase diagram for hard-core bosons on the triangular lattice with nearest-neighbor interactions V and hopping t with density controlled by the chemical potential μ. Identified phases include commensurate solids (at fillings $f = 1/3, 2/3$), superfluid, and supersolid (a superfluid that breaks triangular lattice symmetries). Solid lines indicate discontinuous (first order) transitions, while continuous (second order) transitions occur across dashed lines. The data points in the lower left-hand corner represent the major results of this paper, indicating that the ground state of a single layer of ^{4}He on graphene resides deep in the commensurate solid phase at 1/3 filling. For these data points, the chemical potential has been chosen such that μ/V has the same value as the tip of the first lobe.

5.2 Future Work

Armed with the above realization, we envisage avenues of research that involve effective Bose–Hubbard Hamiltonians of atoms on 2D materials with different lattice parameters. Numerous 2D materials exist, and in addition, their parameters can be affected by external knobs such as strain, doping, etc. These factors also affect the strength of the atom–material potential (which is of van der Waals origin). The ultimate advantage of having a reliable effective Bose–Hubbard description is that it allows studies of strongly correlated phases, such as supersolids, correlated insulators and superfluids, as well as the phase transitions between them. Thus Bose–Hubbard model construction can be viewed as a project of designing low-dimensional physical systems with given correlated

ground state properties, e.g., superfluids in a regime (density, temperature, size) more aligned with conventional solid state physics.

A logical next step in the applications of our methods is exploring the effect of physically straining the Graphene substrate on the location of our results in the phase diagram Fig. 5.1. In straining the graphene substrate, the adsorption potential can still be expressed as Eq. (1.4), though with the lattice vectors $\boldsymbol{a}$ and reciprocal lattice vectors $\boldsymbol{g}$ changed. In addition, the parameters σ and ε must also be changed by fitting $\mathcal{V}_{\mathrm{He-C}}$ to the long distance interactions of a Helium atom with a graphene sheet [18].

The simplest way to strain graphene is isotropic strain, in which the graphene sheet is strained equally in all directions such that the carbon-carbon distance a_0 increases. In this case we expect the hopping parameter t to increase as the sites gets further apart and the Wannier functions to overlap less. We also expect the nearest neighbor interaction V to decrease as the Helium adsorption sites gets further apart. In fact, we expect V to decrease faster as the separation of the sites $\sqrt{3}a_0 = 2.46\text{Å}$ at no strain is close to where the empirical Helium-Helium interaction becomes attractive at $r = 2.65\text{Å}$. With sufficient strain V will in fact become negative. With V decreasing faster than t it is possible that t/V could increase to some value that could indicate superfluidity.

Furthermore, strain could be applied in an anisotropic fashion [18], in which the graphene sheet is strained in only one direction. In this case the Bose-Hubbard model becomes even more complex. The graphene substrate loses its six-fold symmetry and the adsorption potential changes differently along and perpendicular to the axis of strain. In this case, t and V will also become different along and perpendicular to the axis of strain and thus must be calculated separately. This could lead to the possibility of anisotropic superfluid phases, in which the adsorbed Helium becomes superfluid along a single axis.

Bibliography

[1] J. Yu, E. Lauricella, M. Elsayed, K. Shepherd, N. S. Nichols, T. Lombardi, S. W. Kim, C. Wexler, J. M. Vanegas, T. Lakoba, V. N. Kotov, and A. Del Maestro. "Two-dimensional bose-hubbard model for helium on graphene." Phys. Rev. B **103**, 235414 (2021).
URL https://link.aps.org/doi/10.1103/PhysRevB.103.235414

[2] M. Bretz and J. Dash. "Quasiclassical and Quantum Degenerate Helium Monolayers." Phys. Rev. Lett. **26**, 963 (1971).
URL http://journals.aps.org/prl/abstract/10.1103/PhysRevLett.26.963

[3] D. S. Greywall. "Heat capacity and the commensurate-incommensurate transition of He4 adsorbed on graphite." Phys. Rev. B **47**, 309 (1993).
URL https://journals.aps.org/prb/abstract/10.1103/PhysRevB.47.309

[4] J. G. Dash, M. Schick, and O. E. Vilches. "Phases of helium monolayers: search and discovery." Surf. Sci. **299**, 405 (1994).
URL http://www.sciencedirect.com/science/article/pii/003960289490670X

[5] F. M. Gasparini, M. O. Kimball, K. P. Mooney, and M. Diaz-Avila. "Finite-size scaling ofHe4at the superfluid transition." Rev. Mod. Phys. **80**, 1009 (2008).
URL https://journals.aps.org/rmp/abstract/10.1103/RevModPhys.80.1009

[6] L. Reatto, D. E. Galli, M. Nava, and M. W. Cole. "Novel behavior of monolayer quantum gases on graphene, graphane and fluorographene." J. Phys.: Condens. Mat. **25**, 443001 (2013).
URL http://iopscience.iop.org/0953-8984/25/44/443001/

[7] T. Makiuchi, M. Tagai, Y. Nago, D. Takahashi, and K. Shirahama. "Elastic anomaly of helium films at a quantum phase transition." Phys. Rev. B **98**, 235104 (2018).
URL https://journals.aps.org/prb/abstract/10.1103/PhysRevB.98.235104

[8] J. Saunders. "Realizing quantum materials with helium: Helium films at ultralow temperatures, from strongly correlated atomically layered films to topological superfluidity." In "Topological Phase Transitions and New Developments," page 165 (World Scientific, 2018).
URL https://doi.org/10.1142/9789813271340_0012

[9] J. Saunders, B. Cowan, and J. Nyéki. "Atomically layered helium films at ultralow temperatures: Model systems for realizing quantum materials." J. Low Temp. Phys. **201**, 615 (2020).
URL https://doi.org/10.1007/s10909-020-02448-9

[10] M. Kardar. *Statistical Physics of Particles* (Cambridge University Press, 2007). ISBN 9781139464871.

[11] A. Thomy and X. Duval. "Adsorption de molécules simples sur graphite." J. Chim. Phys. **66**, 1966 (1969).
URL https://jcp.edpsciences.org/articles/jcp/abs/1969/03/jcp196966s2p1966/jcp196966s2p1966.html

[12] P. A. Crowell and J. D. Reppy. "Superfluidity and film structure in He4 adsorbed on graphite." Phys. Rev. B **53**, 2701 (1996).
URL https://journals.aps.org/prb/abstract/10.1103/PhysRevB.53.2701

[13] J. Nyéki, R. Ray, G. Sheshin, V. Maidanov, V. Mikheev, B. Cowan, and J. Saunders. "Structure and superfluidity of 4He films on plated graphite." J. Low Temp. Phys. **23**, 379 (1997).
URL https://doi.org/10.1063/1.593382

[14] F. Abraham and J. Broughton. "Phases of helium adsorbed on graphite: A Feynman path-integral Monte Carlo study." Phys. Rev. Lett. **59**, 64 (1987).
URL http://journals.aps.org/prl/abstract/10.1103/PhysRevLett.59.64

[15] M. Pierce and E. Manousakis. "Path-integral Monte Carlo simulation of the second layer of 4He adsorbed on graphite." Phys. Rev. B **59**, 3802 (1999).
URL http://journals.aps.org/prb/abstract/10.1103/PhysRevB.59.3802

[16] M. C. Gordillo and J. Boronat. "Superfluid and Supersolid Phases of He4 on the Second Layer of Graphite." Phys. Rev. Lett. **124**, 205301 (2020).
URL https://journals.aps.org/prl/abstract/10.1103/PhysRevLett.124.205301

[17] A. H. Castro Neto, F. Guinea, N. M. R. Peres, K. S. Novoselov, and A. K. Geim. "The electronic properties of graphene." Rev. Mod. Phys. **81**, 109

(2009).
URL https://link.aps.org/doi/10.1103/RevModPhys.81.109

[18] N. S. Nichols, A. D. Maestro, C. Wexler, and V. N. Kotov. "Adsorption by design: Tuning atom-graphene van der Waals interactions via mechanical strain." Phys. Rev. B **93**, 205412 (2016).
URL http://journals.aps.org/prb/abstract/10.1103/PhysRevB.93.205412

[19] M. Gordillo and J. Boronat. "4He on a Single Graphene Sheet." Phys. Rev. Lett. **102**, 085303 (2009).
URL http://journals.aps.org/prl/abstract/10.1103/PhysRevLett.102.085303

[20] J. Happacher, P. Corboz, M. Boninsegni, and L. Pollet. "Phase diagram of 4He on graphene." Phys. Rev. B **87**, 094514 (2013).
URL http://journals.aps.org/prb/abstract/10.1103/PhysRevB.87.094514

[21] K. S. Novoselov, A. Mishchenko, A. Carvalho, and A. H. Castro Neto. "2D materials and van der Waals heterostructures." Science **353**, 461 (2016).

[22] V. N. Kotov, B. Uchoa, V. M. Pereira, F. Guinea, and A. H. Castro Neto. "Electron-electron interactions in graphene: Current status and perspectives." Rev. Mod. Phys. **84**, 1067 (2012).
URL https://link.aps.org/doi/10.1103/RevModPhys.84.1067http://dx.doi.org/10.1103/RevModPhys.84.1067

[23] M. H. Anderson, J. R. Ensher, M. R. Matthews, C. E. Wieman, and E. A. Cornell. "Observation of bose-einstein condensation in a dilute atomic vapor." Science **269**, 198 (1995).
URL https://science.sciencemag.org/content/269/5221/198

[24] D. C. Aveline, J. R. Williams, E. R. Elliott, C. Dutenhoffer, J. R. Kellogg, J. M. Kohel, N. E. Lay, K. Oudrhiri, R. F. Shotwell, N. Yu, and R. J. Thompson. "Observation of bose–einstein condensates in an earth-orbiting research lab." Nature **582**, 193–197 (2020).
URL https://doi.org/10.1038/s41586-020-2346-1

[25] L. Bruch, M. W. Cole, and H.-Y. Kim. "Transitions of gases physisorbed on graphene." J. Phy.: Condens. Mat. **22**, 304001 (2010).
URL http://iopscience.iop.org/article/10.1088/0953-8984/22/30/304001/meta

[26] M. C. Gordillo, C. Cazorla, and J. Boronat. "Supersolidity in quantum films adsorbed on graphene and graphite." Phys. Rev. B **83**, 121406 (2011).
URL http://journals.aps.org/prb/abstract/10.1103/PhysRevB.83.121406

[27] L. V. Markić, P. Stipanović, I. Bešlić, and R. E. Zillich. "4He clusters adsorbed on graphene." Phys. Rev. B **88** (2013).
URL https://doi.org/10.1103/physrevb.88.125416

[28] W. A. Steele. "The physical interaction of gases with crystalline solids." Surf. Sci. **36**, 317 (1973).
URL https://doi.org/10.1016/0039-6028(73)90264-1

[29] W. E. Carlos and M. W. Cole. "Anisotropic He-C pair Interaction for a He Atom Near a Graphite Surface." Phys. Rev. Lett. **43**, 697 (1979).
URL https://journals.aps.org/prl/abstract/10.1103/PhysRevLett.43.697

[30] W. E. Carlos and M. W. Cole. "Interaction between a he atom and a graphite surface." Surf. Sci. **91**, 339 (1980).
URL https://doi.org/10.1016/0039-6028(80)90090-4

[31] G. Vidali and M. W. Cole. "Effective interaction between He atoms on a graphite surface." Phys. Rev. B **22**, 4661 (1980).
URL https://journals.aps.org/prb/abstract/10.1103/PhysRevB.22.4661

[32] F. Pirani, D. Cappelletti, and G. Liuti. "Range, strength and anisotropy of intermolecular forces in atom-molecule systems: an atom-bond pairwise additivity approach." Chem. Phys. Lett. **350**, 286 (2001).
URL https://doi.org/10.1016/s0009-2614(01)01297-0

[33] F. Pirani, M. Alberti, A. Castro, M. M. Teixidor, and D. Cappelletti. "Atom-bond pairwise additive representation for intermolecular potential energy surfaces." Chem. Phys. Lett. **394**, 37 (2004).
URL https://linkinghub.elsevier.com/retrieve/pii/S0009261404009807

[34] L. Bruch, M. Cole, and E. Zaremba. *Phys. Adsorption: Forces and Phenomena*. Dover Books on Physics (Dover Publications, 2007). ISBN 9780486457673.
URL https://books.google.com/books?id=qZiRDQAAQBAJ

[35] T. L. Badman and J. M. McMahon. "On the Phase Diagrams of 4He Adsorbed on Graphene and Graphite from Quantum Simulation Methods." Crystals **8**, 202 (2018).
URL http://www.mdpi.com/2073-4352/8/5/202

[36] M. Przybytek, W. Cencek, J. Komasa, G. Łach, B. Jeziorski, and K. Szalewicz. "Relativistic and Quantum Electrodynamics Effects in the Helium Pair Potential." Phys. Rev. Lett. **104**, 183003 (2010).
URL https://journals.aps.org/prl/abstract/10.1103/PhysRevLett.104.183003

[37] E. Kaxiras and J. D. Joannopoulos. *Quantum Theory of Materials* (Cambridge University Press, 2019).
URL https://www.cambridge.org/core/books/quantum-theory-of-materials/755973CFD3AA7CF69B3C2380D3F5D16D

[38] C. J. Pethick and H. Smith. *Bose-Einstein condensation in dilute gases* (Cambridge University Press, Cambridge, 2008), 2nd edition.

[39] P. Giannozzi, S. Baroni, N. Bonini, M. Calandra, R. Car, C. Cavazzoni, D. Ceresoli, G. L. Chiarotti, M. Cococcioni, I. Dabo, A. Dal Corso, S. de Gironcoli, S. Fabris, G. Fratesi, R. Gebauer, U. Gerstmann, C. Gougoussis, A. Kokalj, M. Lazzeri, L. Martin-Samos, N. Marzari, F. Mauri, R. Mazzarello, S. Paolini, A. Pasquarello, L. Paulatto, C. Sbraccia, S. Scandolo, G. Sclauzero, A. P. Seitsonen, A. Smogunov, P. Umari, and R. M. Wentzcovitch. "QUANTUM ESPRESSO: a modular and open-source software project for quantum simulations of materials." J Phys Condens Matter **21**, 395502 (2009).
URL https://iopscience.iop.org/article/10.1088/0953-8984/21/39/395502

[40] P. Giannozzi, O. Andreussi, T. Brumme, O. Bunau, M. Buongiorno Nardelli, M. Calandra, R. Car, C. Cavazzoni, D. Ceresoli, M. Cococcioni, N. Colonna, I. Carnimeo, A. Dal Corso, S. de Gironcoli, P. Delugas, R. A. DiStasio, A. Ferretti, A. Floris, G. Fratesi, G. Fugallo, R. Gebauer, U. Gerstmann, F. Giustino, T. Gorni, J. Jia, M. Kawamura, H.-Y. Ko, A. Kokalj, E. Küçükbenli, M. Lazzeri, M. Marsili, N. Marzari, F. Mauri, N. L. Nguyen, H.-V. Nguyen, A. Otero-de-la Roza, L. Paulatto, S. Poncé, D. Rocca, R. Sabatini, B. Santra, M. Schlipf, A. P. Seitsonen, A. Smogunov, I. Timrov, T. Thonhauser, P. Umari, N. Vast, X. Wu, and S. Baroni. "Advanced capabilities for materials modelling with Quantum ESPRESSO." J Phys.: Condens. Matt. **29**, 465901 (2017).
URL https://iopscience.iop.org/article/10.1088/1361-648X/aa8f79

[41] E. Caldeweyher, C. Bannwarth, and S. Grimme. "Extension of the D3 dispersion coefficient model." J. Chem. Phys. **147**, 034112 (2017).
URL https://aip.scitation.org/doi/abs/10.1063/1.4993215?journalCode=jcp

[42] E. Caldeweyher, S. Ehlert, A. Hansen, H. Neugebauer, S. Spicher, C. Bannwarth, and S. Grimme. "A generally applicable atomic-charge dependent London dispersion correction." J. Chem. Phys. **150**, 154122 (2019).
URL https://aip.scitation.org/doi/10.1063/1.5090222

[43] E. Caldeweyher, J.-M. Mewes, S. Ehlert, and S. Grimme. "Extension and evaluation of the D4 London-dispersion model for periodic systems." Phys. Chem. Chem. Phys. **22**, 8499 (2020).

URL https://pubs.rsc.org/en/content/articlelanding/2020/cp/d0cp00502a#!divAbstract

[44] C. Møller and M. S. Plesset. "Note on an Approximation Treatment for Many-Electron Systems." Phys. Rev. **46**, 618 (1934).
URL https://journals.aps.org/pr/abstract/10.1103/PhysRev.46.618

[45] C. Cramer. *Essentials of Computational Chemistry: Theories and Models* (Wiley, 2013). ISBN 9781118712276.
URL https://books.google.com/books?id=k4R6cf7I7q0C

[46] R. J. Bartlett. "Many-Body Perturbation Theory and Coupled Cluster Theory for Electron Correlation in Molecules." Ann. Rev. Phys. Chem. **32**, 359 (1981).
URL http://dx.doi.org/10.1146/annurev.pc.32.100181.002043

[47] N. Gheeraert, S. Chester, M. May, S. Eggert, and A. Pelster. "Mean-Field Theory for Extended Bose-Hubbard Model with Hard-Core Bosons." In G. Wunner and A. Pelster, editors, "Selforganization in Complex Systems: The Past, Present, and Future of Synergetics," (Springer International Publishing, 2016). ISBN 978-3-319-27635-9.

[48] G. Murthy, D. Arovas, and A. Auerbach. "Superfluids and supersolids on frustrated two-dimensional lattices." Phys. Rev. B **55**, 3104 (1997).
URL https://link.aps.org/doi/10.1103/PhysRevB.55.3104

[49] S. Wessel and M. Troyer. "Supersolid Hard-Core Bosons on the Triangular Lattice." Phys. Rev. Lett. **95**, 127205 (2005).
URL https://journals.aps.org/prl/abstract/10.1103/PhysRevLett.95.127205

[50] J.-Y. Gan, Y.-C. Wen, and Y. Yu. "Supersolidity and phase diagram of soft-core bosons on a triangular lattice." Phys. Rev. B **75**, 094501 (2007).
URL https://journals.aps.org/prb/abstract/10.1103/PhysRevB.75.094501

[51] X.-F. Zhang, R. Dillenschneider, Y. Yu, and S. Eggert. "Supersolid phase transitions for hard-core bosons on a triangular lattice." Phys. Rev. B **84**, 174515 (2011).
URL https://journals.aps.org/prb/abstract/10.1103/PhysRevB.84.174515

[52] C. Kittel, H. Charles Kittel, K. Charles, H. Kroemer, and K. Herbert. *Thermal Physics* (W. H. Freeman, 1980). ISBN 9780716710882.

[53] C. E. Campbell, F. J. Milford, A. D. Novaco, and M. Schick. "Helium-Monolayer Completion on Graphite." Phys. Rev. A **6**, 1648 (1972).

URL https://journals.aps.org/pra/abstract/10.1103/PhysRevA.6.1648

[54] P. A. Whitlock, G. V. Chester, and B. Krishnamachari. "Monte Carlo simulation of a helium film on graphite." Phys. Rev. B **58**, 8704 (1998).
URL https://journals.aps.org/prb/abstract/10.1103/PhysRevB.58.8704

[55] G. Zimmerli, G. Mistura, and M. Chan. "Third-sound study of a layered superfluid film." Phys. Rev. Lett. **68**, 60 (1992).
URL http://journals.aps.org/prl/abstract/10.1103/PhysRevLett.68.60

[56] G. Zimmerli and M. H. W. Chan. "Complete wetting of helium on graphite." Phys. Rev. B **38**, 8760 (1988).
URL http://journals.aps.org/prb/abstract/10.1103/PhysRevB.38.8760

[57] Y. Shibayama, H. Fukuyama, and K. Shirahama. "Torsional oscillator studies for possible supersolidity in two-dimensional 4He solid." J. Phys.: Conf. Ser. **150**, 032096 (2009).

[58] S. Nakamura, K. Matsui, T. Matsui, and H. Fukuyama. "Possible quantum liquid crystal phases of helium monolayers." Phys. Rev. B **94**, 180501 (2016).
URL https://doi.org/10.1103/PhysRevB.94.180501

[59] J. Nyéki, A. Phillis, A. Ho, D. Lee, P. Coleman, J. Parpia, B. Cowan, and J. Saunders. "Intertwined superfluid and density wave order in two-dimensional 4He." Nature Phys. **13**, 455 (2017).
URL https://www.nature.com/articles/nphys4023

[60] M. E. Pierce and E. Manousakis. "Role of substrate corrugation in helium monolayer solidification." Phys. Rev. B **62**, 5228 (2000).
URL http://journals.aps.org/prb/abstract/10.1103/PhysRevB.62.5228

[61] J. Ahn, H. Lee, and Y. Kwon. "Prediction of stable C7/12 and metastable C4/7 commensurate solid phases for 4He on graphite." Phys. Rev. B **93**, 064511 (2016).
URL https://journals.aps.org/prb/abstract/10.1103/PhysRevB.93.064511

[62] M. C. Gordillo and J. Boronat. "Zero-temperature phase diagram of the second layer of 4He adsorbed on graphene." Phys. Rev. B **85**, 195457 (2012).
URL http://journals.aps.org/prb/abstract/10.1103/PhysRevB.85.195457

[63] Y. Kwon and D. M. Ceperley. "4He adsorption on a single graphene sheet: Path-integral Monte Carlo study." Phys. Rev. B **85**, 224501 (2012).
URL http://journals.aps.org/prb/abstract/10.1103/PhysRevB.85.224501

[64] M. C. Gordillo. "Diffusion Monte Carlo calculation of the phase diagram of 4He on corrugated graphene." Phys. Rev. B **89**, 155401 (2014).

[65] L. V. Markić, P. Stipanović, I. Bešlić, and R. E. Zillich. "Solidification of 4He clusters adsorbed on graphene." Phys. Rev. B **94**, 045428 (2016).
URL http://journals.aps.org/prb/abstract/10.1103/PhysRevB.94.045428

[66] I. Bloch, J. Dalibard, and W. Zwerger. "Many-body physics with ultracold gases." Rev. Mod. Phys. **80**, 885 (2008).
URL https://link.aps.org/doi/10.1103/RevModPhys.80.885

[67] D. Jaksch, C. Bruder, J. I. Cirac, C. W. Gardiner, and P. Zoller. "Cold Bosonic Atoms in Optical Lattices." Phys. Rev. Lett. **81**, 3108 (1998).
URL https://link.aps.org/doi/10.1103/PhysRevLett.81.3108

[68] R. Walters, G. Cotugno, T. H. Johnson, S. R. Clark, and D. Jaksch. "Ab initio derivation of Hubbard models for cold atoms in optical lattices." Phys. Rev. A **87**, 043613 (2013).
URL https://link.aps.org/doi/10.1103/PhysRevA.87.043613

[69] E. Lifshitz and L. P. Pitaevskii. *Statistical Physics.* Part 2 (Pergamon Press, 1980).

[70] G. D. Mahan. *Many-Particle Physics* (Plenum Press, 1990).
URL https://www.springer.com/gp/book/9780306463389

[71] T. I. Lakoba. "Convergence conditions for iterative methods seeking multi-component solitary waves with prescribed quadratic conserved quantities." Math. Comput. Simul. **81**, 1572 (2011).
URL https://www.sciencedirect.com/science/article/abs/pii/S0378475410003927

[72] A. Sarsa, K. E. Schmidt, and W. R. Magro. "A path integral ground state method." J. Chem. Phys. **113**, 1366 (2000).
URL https://aip.scitation.org/doi/10.1063/1.481926

[73] J. E. Cuervo, P.-N. Roy, and M. Boninsegni. "Path integral ground state with a fourth-order propagator: Application to condensed helium." J. Chem. Phys. **122**, 114504 (2005).
URL https://aip.scitation.org/doi/10.1063/1.1872775

[74] Y. Yan and D. Blume. "Path integral Monte Carlo ground state approach: formalism, implementation, and applications." J. Phys. B: At., Mol. Opt. Phys. **50**, 223001 (2017).
URL http://stacks.iop.org/0953-4075/50/i=22/a=223001?key=crossref.bb4cf3f346cf4f53cc1ead9423aec2dc

[75] A. Del Maestro. "Available online." Del Maestro Group Code Repository (2021). https://code.delmaestro.org.
URL https://code.delmaestro.org

[76] J. Perdew, K. Burke, and M. Ernzerhof. "Generalized Gradient Approximation Made Simple." Phys. Rev. Lett. **77**, 3865 (1996).
URL https://journals.aps.org/prl/abstract/10.1103/PhysRevLett.77.3865

[77] P. Blöchl. "Projector augmented-wave method." Phys. Rev. B **50**, 17953 (1994).
URL https://journals.aps.org/prb/abstract/10.1103/PhysRevB.50.17953

[78] G. Prandini, A. Marrazzo, I. E. Castelli, N. Mounet, and N. Marzari. "Precision and efficiency in solid-state pseudopotential calculations." npj Comput. Mater. **4**, 72 (2018).
URL https://www.nature.com/articles/s41524-018-0127-2

[79] A. Dal Corso. "Pseudopotentials periodic table: From H to Pu." Comput. Mater. Sci. **95**, 337 (2014).
URL https://www.sciencedirect.com/science/article/abs/pii/S0927025614005187

[80] M. Schlipf and F. Gygi. "Optimization algorithm for the generation of ONCV pseudopotentials." Comput. Phys. Comm. **196**, 36 (2015).
URL https://www.sciencedirect.com/science/article/pii/S0010465515001897

[81] M. J. Frisch, G. W. Trucks, H. B. Schlegel, G. E. Scuseria, M. A. Robb, J. R. Cheeseman, G. Scalmani, V. Barone, B. Mennucci, G. A. Petersson, H. Nakatsuji, M. Caricato, X. Li, H. P. Hratchian, A. F. Izmaylov, J. Bloino, G. Zheng, J. L. Sonnenberg, M. Hada, M. Ehara, K. Toyota, R. Fukuda, J. Hasegawa, M. Ishida, T. Nakajima, Y. Honda, O. Kitao, H. Nakai, T. Vreven, J. A. Montgomery, Jr., J. E. Peralta, F. Ogliaro, M. Bearpark, J. J. Heyd, E. Brothers, K. N. Kudin, V. N. Staroverov, R. Kobayashi, J. Normand, K. Raghavachari, A. Rendell, J. C. Burant, S. S. Iyengar, J. Tomasi, M. Cossi, N. Rega, J. M. Millam, M. Klene, J. E. Knox, J. B. Cross, V. Bakken, C. Adamo, J. Jaramillo, R. Gomperts, R. E. Stratmann, O. Yazyev, A. J. Austin, R. Cammi, C. Pomelli, J. W. Ochterski, R. L. Martin, K. Morokuma, V. G. Zakrzewski, G. A. Voth,

P. Salvador, J. J. Dannenberg, S. Dapprich, A. D. Daniels, Ö. Farkas, J. B. Foresman, J. V. Ortiz, J. Cioslowski, and D. J. Fox. "Gaussian 09 Revision E.01." (2009). Gaussian Inc. Wallingford CT 2009.

[82] W. J. Hehre, R. F. Stewart, and J. A. Pople. "Self-Consistent Molecular-Orbital Methods. I. Use of Gaussian Expansions of Slater-Type Atomic Orbitals." **51**, 2657 (1969).